Spring 1-1-2011

Stiffness Analysis of the Tethered Coulomb Structure Concept and Application

Stephen Panosian
University of Colorado at Boulder, stephen.panosian@colorado.edu

Stiffness Analysis of the Tethered Coulomb Structure Concept and Application

by

Stephen Panosian

B.S., The Pennsylvania State University, 2009

A thesis submitted to the

Faculty of the Graduate School of the

University of Colorado in partial fulfillment

of the requirements for the degree of

Master of Sciecne

Department of Aerospace Engineering Sciences

2011

This thesis entitled:
Stiffness Analysis of the Tethered Coulomb Structure Concept and Application
written by Stephen Panosian
has been approved for the Department of Aerospace Engineering Sciences

_____

Hanspeter Schaub

_____

Kurt Maute

_____

Daniel Scheeres

Date _____

The final copy of this thesis has been examined by the signatories, and we find that both the content and the form meet acceptable presentation standards of scholarly work in the above mentioned discipline.

Panosian, Stephen (MS. Aerospace)

Stiffness Analysis of the Tethered Coulomb Structure Concept and Application

Thesis directed by Dr. Hanspeter Schaub

This thesis investigates the Tethered Coulomb Structure (TCS) concept and its operating regime for creating large space structures and for providing satellite situational awareness. A TCS consists of a three-dimensional tethered spacecraft formation that uses electrostatic forces to repel the spacecraft and inflate the formation to a semi-rigid structure. The influential force modeling and equations of motion are given. Numerical simulations of a two-node TCS show that TCS systems have the greatest translational and rotational stiffness when the nodes have high voltage, low separation distance and low mass. Single tether two node TCS at 30 kV with 5 m separation are shown to withstand up to 50 deg/min initial rotations before reaching an entangled state. Multiple tether TCS simulations demonstrate that additional tethers between TCS nodes provides full three-dimensional stiffness and reduces the maximum absolute rotation for the system due to an initial perturbation. Using a double- or triple-tether TCS increases the maximum allowable initial rotation by 40-60%. Orbital perturbations, differential gravity and solar radiation pressure, are examined and it is demonstrated that both can be considered negligible for this study. A TCS configuration where one small spacecraft is tethered to a large spacecraft in orbit is presented. Simulations using a simple attitude control law show that a TCS in this configuration can be used to hold the smaller craft at a relatively fixed arbitrary position and rotation relative to the larger craft. Using multiple tethers for this configuration allows for separation distances of up to 10 m with less than 5 deg and 1 cm relative rotation and translation, respectively.

Dedication

To my family for all their love, support and advice.

Acknowledgements

I have been very lucky to work with many talented and hardworking individuals the past few years and I would like to thank everyone for their help and support. Specifically two people have been of great help that I would like to acknowledge. First, my advisor Dr. Hanspeter Schaub. He allowed me to work on the TCS project and through this work he has taught me the many aspects of research and presentation and technical writing skills that I would ever need. His efforts to teach me and inspire me have definitely impacted my education and I am very grateful for him being my advisor. I would also like to thank my fellow lab mate Carl Seubert. Carl was the previous student working on the TCS concept and was a great help in getting me up to speed with the research. Also, he is always available to bounce ideas off of, help in debugging code and has been a pleasure to work with.

Contents

Chapter

Tables

Table

Figures

Figure

Chapter 1

Introduction

1.1 Motivation and Literature Review

Advancing space technologies such as remote sensing, high resolution surveillance, radiometry, space telescopes, space situational awareness and power collection are pushing the limits of current space based platforms. These technologies desire large space-based platforms on the order of hundreds of meters. Due to launch vehicle fairing size, the space-based platforms for these technologies is currently restricted to free flying spacecraft formations and large space structures that are capable of fitting in a fairing. Advanced space platform technologies with large on orbit shape change ability would allow for hundreds of meter space platforms to be launched on current launch vehicles and perform long duration missions without major fuel restrictions.

One method of creating large rigid space structures is on-orbit construction, which has been demonstrated in recent years by the assembly of the international space station. Even though this method is proven, it requires human or advanced autonomous assembly which is very costly. An additional, less costly, means of large space platforms are deployable spacecraft. This is an active area of research, with only a few being successfully implemented or tested on orbit.[8, 9]

Two proposed NASA missions, Goddard Stellar Imager and the Terrestrial Plantet Finder, have the intent of creating kilometer size baselines in space.[1, 3]. These two missions propose the use of free-flying spacecraft to generate their baseline because these types of formations are capable of variable baselines, system redundancy and fractionated and responsive architectures.[2] However, free-flying formations with their complex relative dynamics have the disadvantage that

they necessitate precise relative motion sensing and control which often requires high propellant usage. Even if the issue of propellant usage can be overcome, whether it be chemical or electrical propulsion, free flying formations are not ideal for proximity operations less than 100 meters. At these lower separation distances, thruster exhaust plume impingement would most likely damage the spacecraft.

Several, essentially propellantless, concepts in recent years that address the relative motion and control issue are to use Coulomb electrostatic interactions,[11, 20] magnetic formation flying,[12] Lorentz forces,[18] or flux-pinning.[6] Of specific interest is the use of inter-spacecraft Coulomb forces to conduct close formation relative control because of its low power and propellant requirements.[11, 20, 21] Even with the benefits this technology provides, the control of such a cluster of spacecraft remains a challenging area of research because of the non-affine nature of electrostatic force actuation. Only two and three craft formations have had analytically stable charge feedback control strategies developed.[15, 16, 17, 29] Additionally, Coulomb spacecraft have been proposed for the self-assembly of large space structures.[10] However, there are no analytical stability guarantees for this $N-$vehicle assembly. This work examines a new concept, the Tethered Coulomb Structure, that addresses the pitfalls of other space based technologies.

1.2 Tethered Coulomb Structure Concept

A novel new technology called the Tethered Coulomb Structure (TCS) provides a means of creating large space structures using Coulomb forces and spacecraft interconnected with tethers.[22, 24] Compared to the previously mentioned free-flying Coulomb spacecraft, a TCS provides the added benefit that the relative translation and rotation of spacecraft is restricted by the length and attachment point of the interconnecting tethers. Figure 1.1 illustrates the TCS concept where individual spacecraft nodes are interconnected with fine, low-mass tethers. Electrostatic (Coulomb) forces provide repulsion between nodes when the spacecraft have the same polarity. The Coulomb forces inflate the TCS structure and provide structure rigidity while the shape and size of the TCS is determined by the tether lengths and attachment points. However, it is envisioned that tether

lengths could be varied on orbit. The potential on the spacecraft that creates the Coulomb forces is obtained by using charge control devices. Active ejection of ions or electrons is used to drive a spacecraft's potential away from its natural space weather dependent equilibrium to the desired potential.

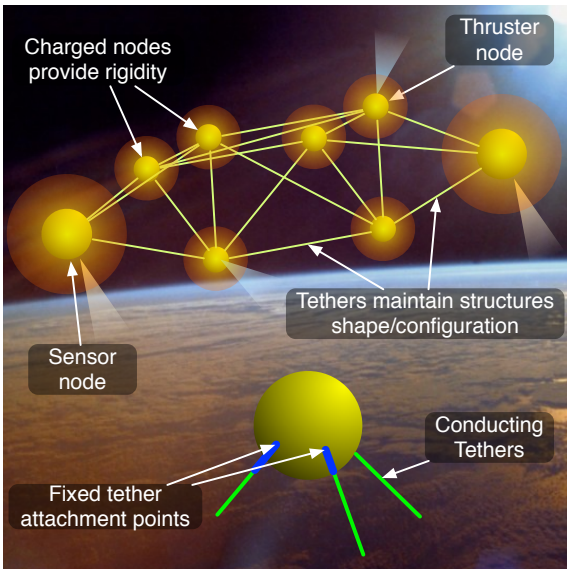

Figure 1.1: Tethered Coulomb Structure concept

Some key advantages of a TCS is that it would have long term mission capability because, like Coulomb formation flying, it only requires Watt-levels of power and little propellant mass.[22] The major benefit of a TCS compared to Coulomb formation flying is that the control required for TCS is substantially reduced. TCS systems do not require precise charge levels to maintain relative positions due to their shape being constrained by the tethers. Spacecraft charge levels must only be maintained above a certain threshold for which the TCS system would be robust to orbital perturbations such as differential gravity and solar radiation pressure. Additionally, relative attitude control between spacecraft nodes will be negligible when the Coulomb and tensile forces are in equilibrium.

It is envisioned that TCS configuration sizes will vary from two-node five-meter systems to many node systems of hundreds of meters. Large TCS sizes are possible because the TCS concept has the benefit of being able to be launched in a compact configuration and then deployed

on-orbit. The deployment is controlled by the Coulomb inflationary forces which then provide structural rigidity. The TCS shape is determined by the length of the tethers, but varying mission sensing requirements could be accommodated with length-adjustable tethers. The TCS concept is not restricted to large space structures but can also be used to hold a small spacecraft in a reasonably fixed position relative to a primary spacecraft. This provides a means for situational awareness or other local sensing. Additionally, a TCS system is not restricted to specific equilibrium configurations or spin rates because the Coulomb force can be used to maintain tension in the tether.

Figure 1.2 shows how the TCS concept compares to other space platform technologies. Specifically, it shows the relation between a systems on-orbit shape change ability and the required control for that technology. Starting in the lower left of the figure is a large monolithic spacecraft, such as the Hubble space telescope, which is a single structure with its only shape change ability being that it can deploy solar panels on orbit. This technology requires minimal relative motion or structure flexing control. Next in the figure is large deployable space structures. The iSat is one envisioned large deployable spacecraft in which the structure could reach a 100 meters or larger. These types of structures would have minimal mass and could require active damping to remove oscillations. Continuing on, other larger structures such as solar sails, inflatable spacecraft then tethered spacecraft allow for more on-orbit shape change but would require more active control. On the far right of the figure is free-flying formations. This technology provides immense amount of variation of orbit shape, that is only limited to propulsion and fuel constraints. Even so, the relative sensing and control would have to be much greater than any of the previous technologies. The proposed TCS concept lies between a tethered spacecraft and free-flying formations. The shape change of a TCS is only limited by the tether connection points and tether lengths. The nodal control is vastly simplified because the Coulomb inflation and tensile forces bound the relative positions and rotations.

Compared to the other spacecraft technologies in Figure 1.2, the TCS concept has one additional constraint, the local plasma environment. TCS systems must operate at GEO altitudes or higher where the local plasma is nominally hot and sparse so that there is minimal charge shielding

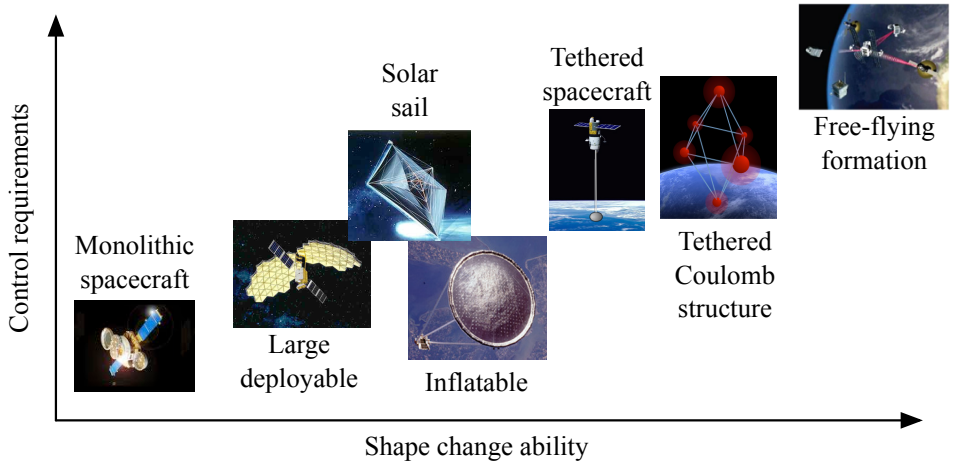

Figure 1.2: TCS concept shape change attributes and control requirements comparison

due to the local plasma. Charge shielding effectively reduces the repulsion forces between spacecraft nodes which in more cold and dense plasma could cause a TCS to collapse. During Earth eclipse at GEO, spacecraft can naturally charge to kilovolt potentials. These such levels are what is envisioned for a TCS.[4, 13] Additionally, there is space-proven technology that could control the charge of a spacecraft with a charge-emission device. This charge control, at the volt-level, was demonstrated on the European CLUSTER mission.[5, 27, 28] Since the spacecraft are all interconnected, a charge control device could be used on all structures or only on one craft and then distributed via conducting tethers. The advantages and disadvantages of either charging scenario are still being researched.

Previous research on the TCS concept investigates relative motion without nodal rotation[22] as well as simplified two-dimensional translational and rotational motion about one axis.[24]. This research expands upon previous work to investigate and quantify the full three-dimensional translational and rotational stiffness of a TCS using numerical simulations. Due to the high non-linearity of a TCS, only numerical simulations are conducted. The stiffness of a two node TCS system is used for analysis because it represents a lower bound on a TCS systems stiffness. TCS system properties and effects of multiple tethers between nodes are examined to determine optimal TCS configuration characteristics. Finally, this work presents and analyzes a TCS application in which a

small spacecraft is tethered to a large spacecraft at GEO to determine the feasibility and operating regimes of using the TCS concept for satellite self situational awareness.

1.3 Outline

The work in this thesis explores the fundamentals of the TCS concept and its application. To begin, an explanation of the the electrostatic force model that is used in simulation is given. This is followed by the definition of the other influential forces and the presentation of the full translational and rotational equations of motion. Next the translational and rotation stiffness of a two node TCS is analyzed. Specifically, the effects of system and nodal parameters are examined as well as environmental impacts. The impact and benefit of multiple tethers between TCS nodes is then presented. From here, the expected perturbations for a TCS and their impact are evaluated. Following that, a specific application for a TCS is introduced in which a small TCS node is attached to a larger node at GEO. Lastly, the final results from this work are presented and future work ideas are given.

Chapter 2

Tethered Coulomb Structure Equations of Motion

2.1 Electrostatic Force Modeling

A Coulomb force is generated from the electrostatic interaction of two charged bodies. If two bodies in a vacuum have charges q_1 and q_2, the Coulomb force between them is computed as:

$$|\boldsymbol{F}_c| = k_c \frac{|q_1 q_2|}{r_{12}^2} \tag{2.1}$$

where $k_c = 8.99 \times 10^9$ $\mathrm{Nm^2C^{-2}}$ is the vacuum Coulomb constant and r_{12} is the separation distance between bodies 1 and 2. If it is assumed that the spacecraft body is comprised of an outer spherical surface that maintains a constant charge q_1, then its potential in a vacuum is given as:

$$V_{sc1} = \frac{q_1 k_c}{\rho} \tag{2.2}$$

where ρ is the radius of the spherical craft.

Equation 2.2 is only valid in a vacuum, which is not true at GEO. At GEO, the Coulomb force will be partially shielded by free-flying charged particles of the local plasma environment. The Debye length, λ_D, signifies the strength of the shielding due to the plasma. If a small spacecraft potential compared to the local plasma thermal energy is assumed

$$e_c V_{sc1} \ll \kappa T_e \tag{2.3}$$

where $e_c = 1.602176 \times 10^{-19}$ C is the elementary charge, $\kappa = 1.38065 \times 10^{-23}$ $\mathrm{JK^{-1}}$ is the Boltzmann constant and T_e is the plasma electron temperature in Kelvin, then the potential about this charged

craft is represented by the Debye-Hückel equation [7, 30]:

$$V = k_c \frac{q_1}{r} e^{-(r-\rho)/\lambda_D} \tag{2.4}$$

This potential equation incorporates plasma shielding and represents a conservative bound of the charge interaction the nodes will experience[14]. At GEO, the $e_c V_{sc1} \ll \kappa T_e$ condition is no longer true if the spacecraft charges to 1-10 kV potentials. The neglected higher order terms of Poisson's partial differential equation, which led to Equation 2.4, results in less plasma shielding of the electrostatic fields.[14] Thus, the use of Equation 2.4 is considered a conservative estimate of the actual potential that might exist about a body. The benefit of using Equation 2.4 is that it allows for simplified analysis, and faster numerical simulations because the full Poisson-Vlasov equations do not need to be solved. Solving the full Poisson-Vlasov equations requires solving complex partial differential field equations.

Taking the gradient of the potential in Equation 2.4 (assuming spherical symmetry) yields the resulting Coulomb force $\boldsymbol{F}_c$ relationship between charged craft 1 and 2:

$$|\boldsymbol{F}_c| = k_c \frac{q_1 q_2}{r_{12}^2} e^{(-(r_{12}-\rho))/\lambda_D} \left(1 + \frac{r_{12}}{\lambda_D}\right) \tag{2.5}$$

The Coulomb force of Equation 2.5 is created between two point charges and does not accommodate realistic charge distribution effects from having two closely separated finite spheres. An improvement to the Coulomb force is made by modeling the effective charge between two finite spheres of fixed potential. This has a significant influence on the effective charge of each sphere when the center-to-center separation is low relative to the sphere radii (separations less than approximately 10 sphere radii, $r < 10\rho$). Figure 2.1 shows two close spheres that maintain a fixed potential, V_i.

In the absence of sphere 2, the point charge of 1 is computed using Equation 2.2. However, once sphere two is introduced the net potential of both spheres changes the effective sphere charge and consequently the Coulomb force. The potential at sphere 1 is computed including the charge of sphere 2 using the expression[25, 26]:

$$V_1 = k_c \frac{q_1}{\rho} + k_c \frac{q_2}{r} \tag{2.6}$$

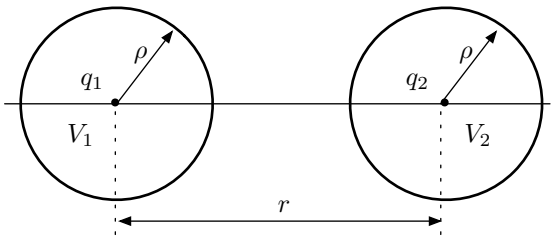

Figure 2.1: Two closely separated charged finite spheres

Similarly, there is an equivalent potential equation for sphere 2. With spheres 1 and 2 set to known and equivalent potential magnitudes $V_1 = V_2$, (a nominal TCS application characteristic) the two potential equations can be independently solved for the resulting equivalent charge of each sphere:

$$q_i = \frac{V_i}{k_c}\left(\frac{\rho r}{\rho + r}\right) \tag{2.7}$$

If the spheres have a large separation distance ($r \gg \rho$) Equation 2.7 will reduce to the standard single sphere charge defined in Equation 2.2, as required. The effective charge and repulsive Coulomb force is reduced from the equivalent point charge model. Using the charges from this model and the force equation of Equation 2.5 is a conservative estimate for the force in a plasma. Modeling electrostatic forces between two finite spheres in a plasma is still under investigation.

Generalizing Equation 2.6 for N spheres gives the potential equation:

$$V_i = k_c\left(\frac{q_i}{\rho_i} + \sum_{j=1}^{N}\frac{q_j}{r_{ij}}\right) \quad j \neq i \tag{2.8}$$

Equation 2.8 can be reduced to a system of linear equations given by:

$$\boldsymbol{V} = k_c A \boldsymbol{q} \tag{2.9}$$

where A is given by:

$$A = \begin{bmatrix} \frac{1}{\rho_1} & \frac{1}{|r_{12}|} & \cdots & \frac{1}{|r_{1N}|} \\ \frac{1}{|r_{12}|} & \frac{1}{\rho_2} & & \vdots \\ \vdots & & \ddots & \vdots \\ \frac{1}{|r_{1N}|} & \cdots & \cdots & \frac{1}{\rho_N} \end{bmatrix} \tag{2.10}$$

This system of equations is what is used in simulation to solve for the charges of each node.

2.2 TCS Forces

The numerical simulation used for this research solves for the translational and rotational motion of TCS nodes. The only forces assumed to be acting on a TCS at GEO are Coulomb, tensile, gravity, and solar radiation pressure forces. The Coulomb force is given in the previous sections by Equations 2.5 and 2.8. The remaining forces are discussed here.

The tethers are modeled as a proportional spring with nonlinear end displacements. This allows for general tether stretching due to arbitrary node translation and/or rotation. The magnitude of the tensile force from a single tether is given by:

$$|\boldsymbol{F}_{\mathrm{s}}| = \begin{cases} k_{\mathrm{s}}\delta L & \delta L > 0, \\ 0 & \delta L \leq 0. \end{cases} \tag{2.11}$$

where k_s is the proportional spring constant and δL is the stretch in the tether. The spring constant is given by:

$$k_s = \frac{EA}{L} \tag{2.12}$$

where E, A and L are Young's modulus, tether cross-sectional area and the nominal tether length, respectively. For this work E and A are assumed to be $271e9Pa$ and $5.29e-10m^2$, respectively. These values are representative of materials that are being consider for the TCS tethers.

If only a two node TCS with a single there is simulated, Equation 2.11 would give the total tether force on a node. However, the simulation is capable of simulating more than two nodes with multiple tethers between nodes. The NxN adjacency matrix, $[K]$, defines which nodes are connected and by how many tethers, where N is the number of spacecraft nodes. The tether length increase of tether k between nodes i and j is defined by δL_{ijk}. Therefore, the resulting tensile force acting on node i from the tether(s) connected to node j is:

$$\boldsymbol{T}_{ij} = k_{\mathrm{s}} \sum_{k=1}^{M} \delta L_{ijk} \hat{\boldsymbol{\tau}}_{ijk} \tag{2.13}$$

where M is the number of tethers between nodes i and j as defined by $[K_{ij}]$ and $\boldsymbol{\tau}_{ij}$ is the vector defining the k^{th} tether's connections between node i to j.

A two-body model for gravity is used in simulation to simulate a TCS operating on orbit at GEO. The force from gravity is given as:

$$|\boldsymbol{F}_g| = \frac{\mu m_i}{|\boldsymbol{R}_i|^2} \tag{2.14}$$

where $\mu = 3.986 \times 10^{14}$ m^{3}s^{-2} is the gravitational coefficient for Earth, m_i is the spacecraft node mass and $\boldsymbol{R}_i$ is the inertial position of node i.

Solar radiation pressure is simulated using a simplified model. The SRP force magnitude is given by:

$$F_{srp} = P_{srp} C_r A_{sc} \tag{2.15}$$

where P_{srp}, C_r, and A_{sc} are the solar radiation pressure, surface reflectivity of the spacecraft and the cross-sectional area of the spacecraft, respectively.

2.3 Translational Equations of Motion

All four forces presented previously impact the translational motion of a TCS node. Including gravity and solar radiation pressure, then summing over all nodes, including the Coulomb force of Equation 2.5 and the tensile force of Equation 2.13, results in translational equations of motion of node i being calculated by:

$$\ddot{\boldsymbol{R}}_i = -\frac{\mu}{|\boldsymbol{R}_i|^2}\hat{R}_i + P_{srp} C_r A_{sc} \hat{S}_i + \sum_{j=1}^{N} K_{ij} \frac{\boldsymbol{T}_{ij}}{m_i} + \sum_{j=1}^{N} \frac{k_c q_i q_j (-\hat{\boldsymbol{r}}_{ij})}{m_i r_{ij}^2} e^{(-(r_{12}-\rho))/\lambda_D} \left(1 + \frac{r_{ij}}{\lambda_D}\right) \quad , \quad i \neq j \tag{2.16}$$

where $\hat{R}_i$ is the unit vector from the Earth to node i, $\hat{S}_i$ is the unit vector from the Sun to node i, N is the total number of nodes in the TCS model, and K_{ij} is a scalar based on the adjacency matrix which is 0 if no tethers connected or 1 if any tethers are connected. Figure 2.2 depicts a general multi-node TCS with various amounts of tethers which is governed by Equation 2.16. Equation 2.16 is the full translational motion for a TCS in GEO. However, most of the simulations in this work use a simplified model for translational motion where gravity, solar radiation pressure

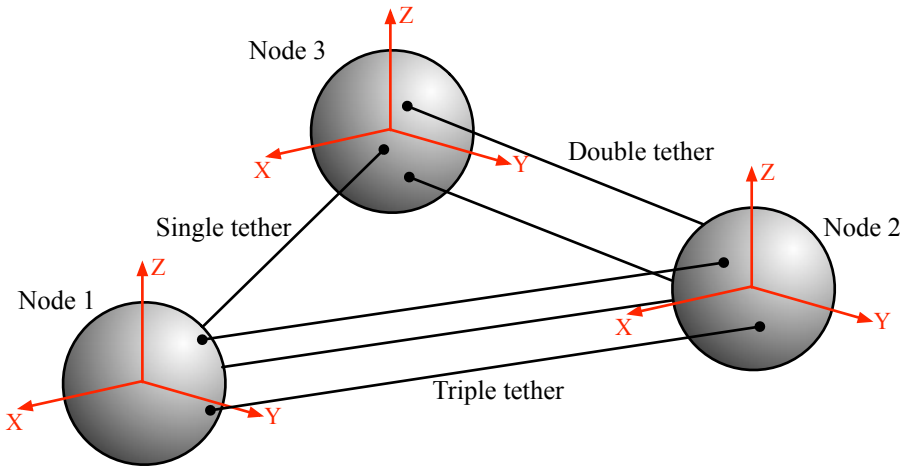

Figure 2.2: Dynamic model setup for a 3D three-node example

and plasma effects are neglected. The simplified equation of motion is given by:

$$\ddot{\boldsymbol{R}}_i = \sum_{j=1}^{N} K_{ij} \frac{\boldsymbol{T}_{ij}}{m_i} + \sum_{j=1}^{N} \frac{k_c q_i q_j (-\hat{\boldsymbol{r}}_{ij})}{m_i r_{ij}^2} \quad , \quad i \neq j \tag{2.17}$$

Justification for this simplification is given in further sections.

2.4 Rotational Equations of Motion

It is assumed that the only force that affects the rotational motion of a TCS are the tether forces. Coulomb forces are neglected because they are assumed to be acting on the center of each node. Differential gravity can be ignored because the spacecraft are spherical. Solar radiation pressure can induce torques but its effects are not included here. Justification for this is given in a later section. Therefore, the attitude of each spacecraft node is dependent on the torque acting on the node from each tether:

$${}^{\mathcal{B}}\boldsymbol{\Gamma}_i = \sum_{j=1}^{N} \left[\sum_{k=1}^{M} \left(K_{ij} {}^{\mathcal{B}}\boldsymbol{p}_{ijk} \times [\mathcal{BI}]_i {}^{\mathcal{I}}\boldsymbol{T}_{ijk} \right) \right] \quad , \quad i \neq j \tag{2.18}$$

where $\boldsymbol{p}_{ijk}$ is the body fixed vector that defines the location of the k^{th} tether attachment point on node i that connects to node j and $[\mathcal{BI}]_i$ is the direction cosine matrix of the attitude of node i relative to the inertial frame. The angular acceleration of each node is defined in the body frame

with Euler's rotational equations of motion[19]:

$$[I]\dot{\boldsymbol{\omega}}_i = -\boldsymbol{\omega}_i \times ([I]\boldsymbol{\omega}_i) + \boldsymbol{\Gamma}_i \tag{2.19}$$

The attitude of each node is represented with the modified rodrigues parameters (MRP) which are integrated using the differential kinematic equation:

$$\dot{\boldsymbol{\sigma}}_i = \frac{1}{4}\left[(1-\sigma_i^2)[I_{3x3}] + 2[\tilde{\boldsymbol{\sigma}}]_i + 2\boldsymbol{\sigma}_i\boldsymbol{\sigma}_i^T\right]\boldsymbol{\omega}_i \tag{2.20}$$

The MRP set will go singular with a rotation of $\pm 360°$. To ensure a non-singular description, the MRP description is switched to the shadow set whenever $|\boldsymbol{\sigma}| > 1$.[19]

Chapter 3

Translational and Rotational Stiffness

3.1 Translational Stiffness

Using the TCS equations of motion, a simplified two-node TCS configuration is numerically simulated using Equation 2.17 to study the effects of various system parameters on the translational stiffness of the TCS. Simulation validation can be found in Appendix A. The system parameters under investigation are the node separation distance, node mass, tether spring constant and node voltage. Table 3.1 shows the nominal parameters used in the numerical simulation sweeps. These parameters are the values used when varying the other parameters. Figure 3.1 shows the translational frequency and peak to peak oscillation amplitude for the various simulations conducted. For these simulations the nodes are started with the tensile and Coulomb forces in equilibrium and then each node is given and equal and opposite initial translational velocity of 0.1 mm/s.

Figure 3.1 illustrates the common trends of a two node configuration as the TCS parameters are varied. For example, Figures 3.1(a), 3.1(b), 3.1(c), and 3.1(d) show the frequency and amplitude response if the voltage and separation distance is varied and all other parameters are held fixed.

Table 3.1: Translational simulation parameters

Separation Distance	5 m
Node Mass	50 kg
Spring Constant	35.8398 N/m
Node Voltage	30 kV

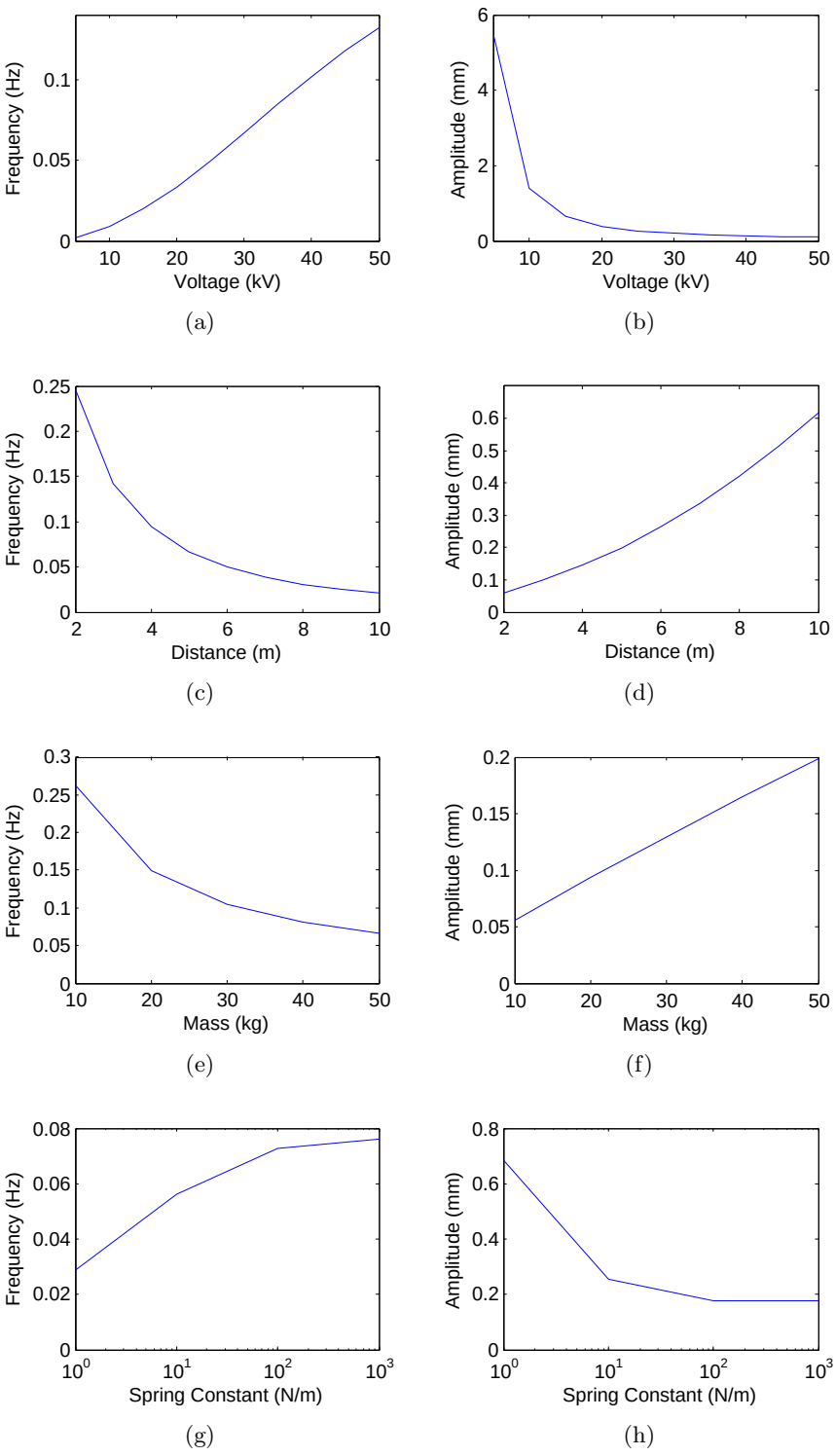

Figure 3.1: Translational motion dependencies.

Naturally the translational frequency and the amplitudes vary as the TCS equilibrium depends on the voltage and separation distance used. The figure shows that larger voltages and shorter separation distances increase the translational stiffness.

Figures 3.1(e) and 3.1(f) show how the translational stiffness increases if the nodal masses are kept small. Thus, for the TCS concept, it is beneficial to keep the support nodes as light as possible to increase the translational TCS stiffness. Additionally, Figures 3.1(g), 3.1(h) show that a stiffer tether provides more translational stiffness.

3.2 Rotational Stiffness

Rotation of individual nodes is of specific interest for TCS systetms because the rotational stiffness will have direct effects on deployment and orbital maneuvers of TCS systems. The aim of this section is to determine the allowable rate and direction of node rotation that will return the node to its original attitude and that which does not result in the tether becoming entangled with the node. A TCS configuration must be robust towards initial conditions and perturbations. Therefore the rotational stiffness of a two node configuration in deep space (no gravity) is examined. Figure 3.2 details a rotation scenario that is studied. This scenario is chosen because there is no net angular momentum, thus isolating the effects of TCS system parameters. Please note that this 2-node, single-tether configuration provides the worst possible rotational stiffness of a TCS system. As such, it is a good system to study to examine lower performance bounds. This section examines the two-node TCS for various TCS parameters and initial rotation rates. Additionally, the impact of nodal properties such as inertia and nodal radius is examined.

3.2.1 System Parameter Effects

Similar to the translational stiffness analysis, a two-node TCS is examined for various voltages, masses, separation distances and spring constants. The rotational case shown in Figure 3.2 is simulated with the parameters shown in Table 3.2, and the resulting rotational frequencies and maximum angular deflections are shown in Figure 3.3. For these simulations the nodes are started

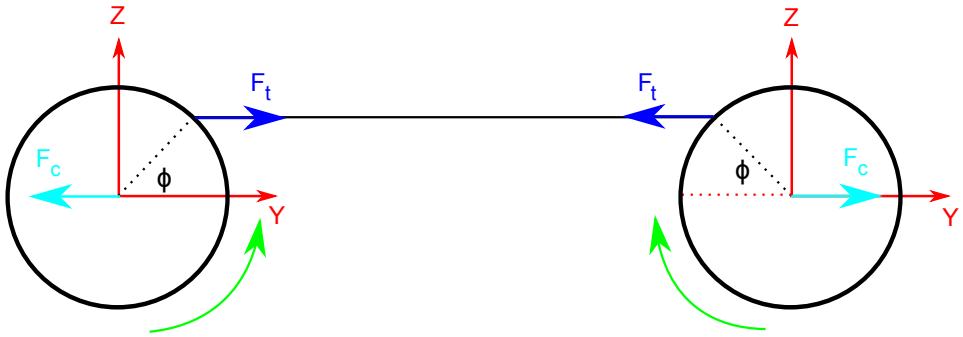

Figure 3.2: Asymmetric rotational motion

at a TCS equilibrium with an initial angular spin rate of 10 deg/min.

Figures 3.3(a) and 3.3(c) show that the rotational stiffness of a TCS configuration can be increased by decreasing either the node mass and/or decreasing the node separation distance. Additionally, Figures 3.3(b) and 3.3(d) show that decreasing the separation distance and/or node mass also decreases the maximum deflection of the nodes. Figures 3.3(e) and 3.3(f) illustrate that the spring constant has little effect on the rotational stiffness of a TCS configuration. Finally, Figures 3.3(g) and 3.3(h) show that increasing the node voltage effectively increases the TSC system rotational stiffness.

Even though these cases are a lower bound on TCS performance, Figure 3.4 shows that the spacecraft are still capable of withstanding moderate initial rotation rates without the tether wrapping up around the spacecraft. For this single tether spherical two-node TCS, tether wrap up would occur when a node is rotated 90 degrees from the vector connecting the two nodes. Figure 3.4(a), 3.4(b) and 3.4(c) show the maximum angular deflection of nodes over various initial rotation rates and voltages for 2.5m, 5m, and 10m separation distances. The results from Figure 3.4 also agree with the results from Figure 3.3, which show that larger voltages and shorter separation distances increase the rotational stiffness of the TCS configuration.

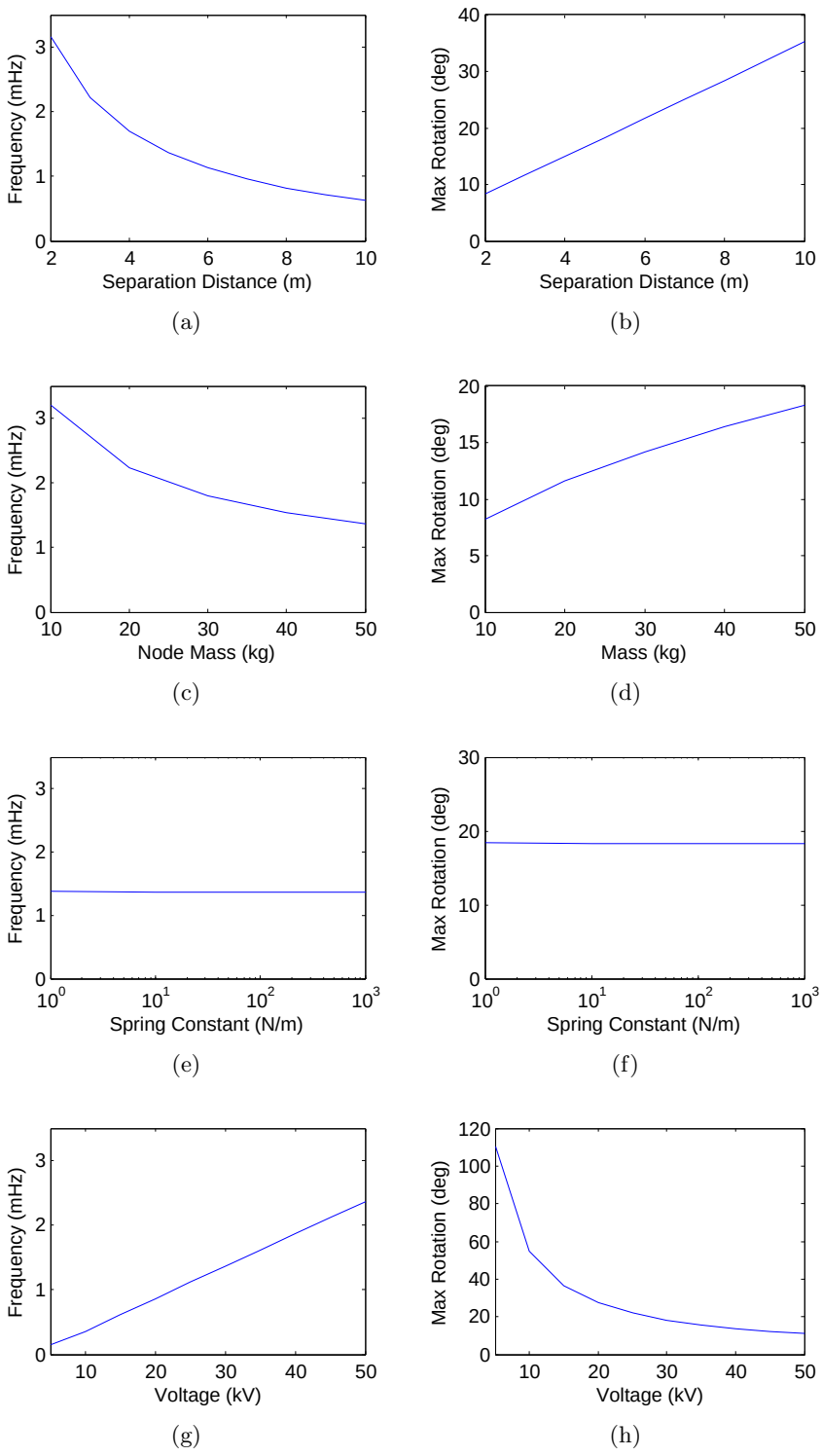

Figure 3.3: Rotational motion dependencies.

Table 3.2: Rotational simulation parameters

Separation Distance	5 m
Node Mass	50 kg
Spring Constant	35.8398 N/m
Node Charge	30 kV
Node Radius	0.5 m
Inertia Distribution	Solid Sphere

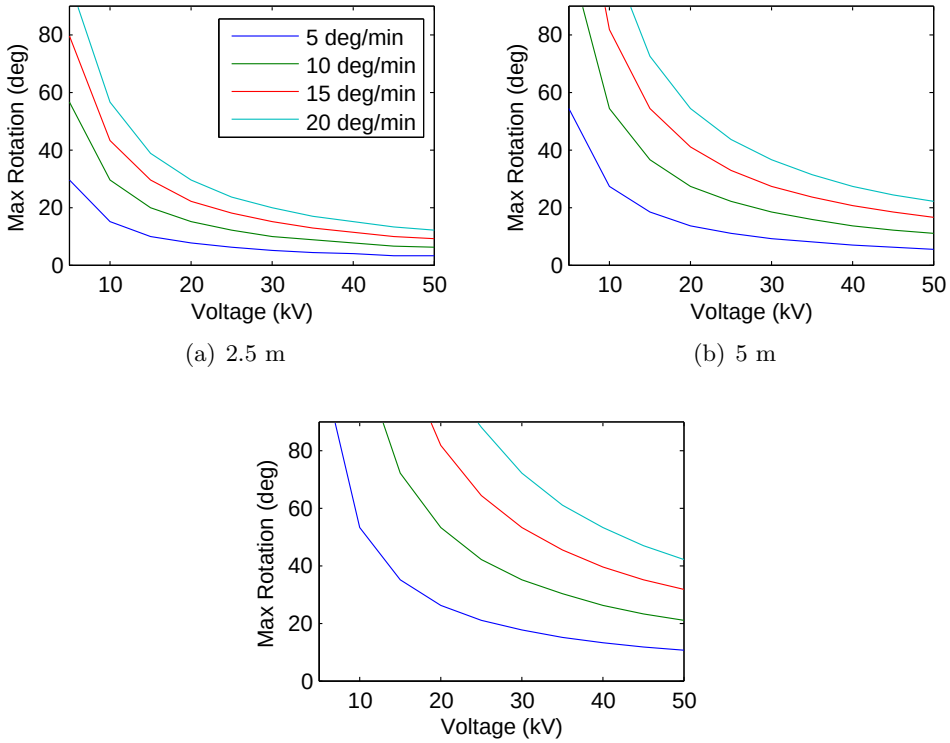

(a) 2.5 m

(b) 5 m

(c) 10 m

Figure 3.4: Stiffness towards initial spin rates

3.2.2 Spacecraft Nodal Properties

To further expand the TCS capabilities it is advantageous to explore other system parameters that affect the rotational stiffness of the system. Spacecraft nodal parameters such as radius and mass distribution are critical components in determining the rotational stiffness of a TCS configuration. Figure 3.5 shows the effect of varying these nodal parameters on the maximum

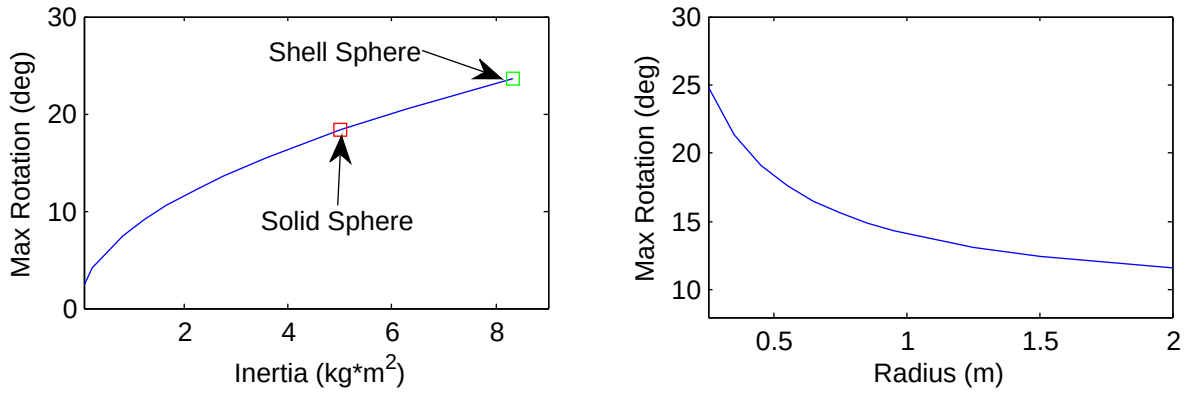

(a) Variation in nodal mass moment of inertia

(b) Variation in node radius

Figure 3.5: Node parameter variation

absolute rotation of a two-node configuration, disturbed about the X-axis. During the inertia variation, the mass and radius are held fixed. For the radius variation, the inertia is based off of the radius. Figures 3.5(a) and 3.5(b) show the results for a single-tether TCS as a function of mass distribution and nodal radii respectively. All other simulation parameters are listed in Table 3.2.

With a node of a certain mass and radius, the shell model provides the largest possible nodal inertia. This scenario is the lower bound on the rotational stiffness that can be achieved. The solid sphere (homogeneous mass distribution throughout the sphere) will have a lower inertia, and thus increased rotational stiffness. However, even the solid sphere model is very conservative. Ideally the TCS nodes would have most of their mass near the node center, and thus obtain an even lower moment of inertia. As Figure 3.5(a) indicates, compared to the shell model, a 2-3 fold increase in the rotational stiffness can be achieved by designing the TCS nodes to have their most massive components near the nodal center, and thus a lower inertia. Additionally, for a constant mass distribution, solid sphere, Figure 3.5(b) shows that larger node radii increase the rotational stiffness. Even though the inertia is increasing for larger radii, the larger moment arms for the tether dominates and thus increases the stiffness. Therefore, Figure 3.5(b) indicates that the ideal TCS would have its attachment point the furthest away from the center of the craft.

Taking into consideration the previous results of nodal parameters an ideal TCS spacecraft

node design may appear similar to the conceptual illustration of Figure 3.6. The figure depicts a multiple tether TCS, whose detailed effects are discussed in a later section. However, multiple tether TCS have the same dependencies on inertia and radius. This design maximizes the spacecraft rotational stiffness, increases nodal wrap-up angles and provides a spherical conductive surface for even Coulomb force generation. The mass moment of inertia is minimized by placing the spacecraft components within a low-mass exterior conducting shell. The tethers are connected to attachment arms that extend beyond the shell increasing the tether moment arms and consequently rotational stiffness. This attachment arm design also increases the maximum angle before nodal wrap up.

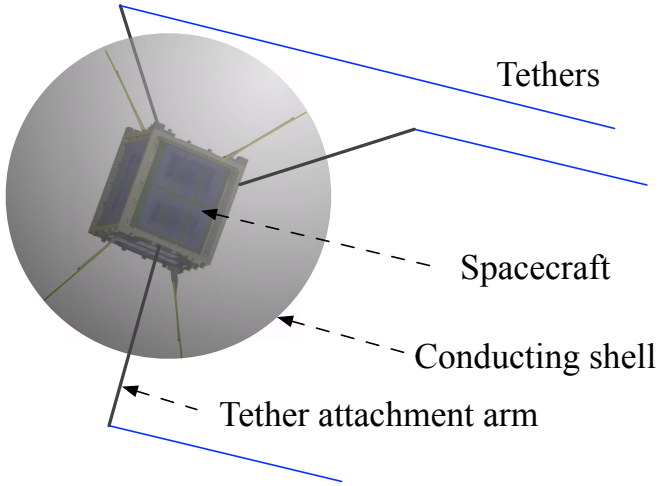

Figure 3.6: Illustration of conceptual TCS spacecraft node design

3.3 Environmental Impacts on Stiffness

Analyzed here is the effect of charge shielding which reduces the inflationary Coulomb force and stiffness capabilities of the system.[24] The charge reduction is examined for a range of GEO Debye lengths from nominal to worst-case conditions. Figure 3.7 shows the effect of these plasma conditions on the rotational stiffness of a single-tether TCS configuration with disturbance about the X-axis. The results shown are for the conservative partial charge shielding force model of Equation (2.5). For spacecraft charges of these magnitudes, the effective Debye length will in fact be larger improving the rotational stiffness results.

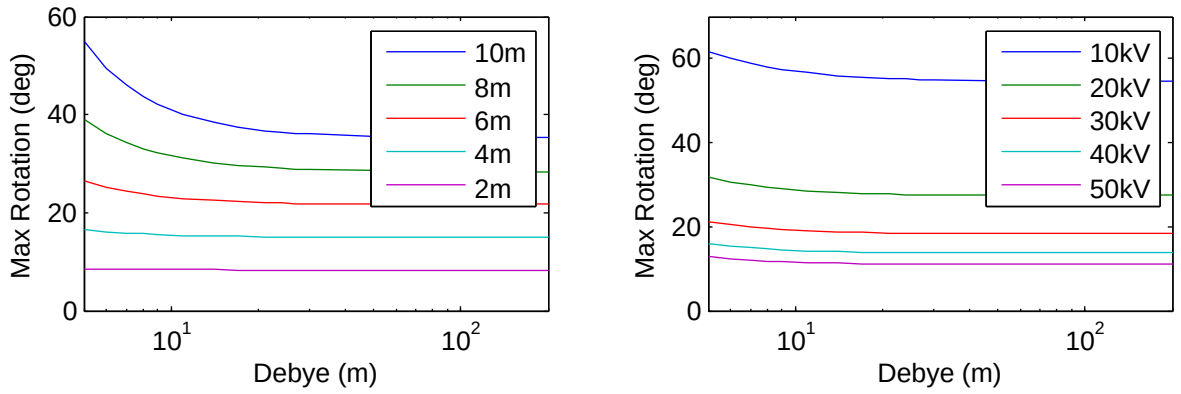

(a) Variation in nodal separation

(b) Variation in nodal potential

Figure 3.7: Maximum absolute principal rotation as a function of environmental conditions (Debye length)

Figure 3.7 shows that environmental conditions have minimal impact on the dynamics of a closely-operated TCS system until Debye lengths on the order of 10 meters or smaller are considered. The maximum absolute rotation lines in the figures converge to the maximum rotation values with no plasma shielding. Nominal values of Debye lengths (far right of figure) have no effect, but as the plasma Debye length reduces to the worst case value the rotational stiffness decreases. When designing for the worst case plasma conditions, consideration must be made for TCS nodal separations larger than 5 meters. Considering a TCS system with a large number of nodes spanning 100 meters, the shorter Debye length plasma shielding will also impact the overall rigidity of this system. The results in Figure 3.7 are specific to a simple two-node system and short separations.

Chapter 4

Multiple Tether TCS

4.1 Multiple Tether Configurations

A key thing to note about rotation of single-tether two-node TCS is that it does not provide full three-dimensional stiffness. Figure 3.2 shows that initial rotations about the Y-axis would have no restoring torque. One way to provide the desired three-dimensional stiffness is to interconnect the nodes with two or three tethers. The connections for these scenarios are shown in Figure 4.1.

However, the addition of tetheres does affect the rotation angle at which a node will become entangled with a tether. The variation in entanglement angles can be seen for the double- and triple-tether TCS configurations in Figure 4.1. Table 4.1 lists the nodal rotation angles at which each TCS configuration will reach the entangled state. The entanglement rotations in Table 4.1 are based upon geometry, where $\theta = \tan^{-1}(2\cot\phi)$ and $\psi = \tan^{-1}\left(2\cot\phi/\sqrt{3}\right)$. However, one should note that nodes are not likely to be spherical and the tether attachment points could be attached away from the nodes on booms, thus increasing the possible absolute rotations.

Table 4.1: Spherical node rotation causing tether entanglement (for single-axis, asymmetric rotations)

Rotation Axis	Single-Tether (deg)	Double-Tether (deg)	Triple-Tether (deg)
X-axis (Node 1 Positive)	90	90 - ϕ	90 - θ
X-axis (Node 1 Negative)	90	90 - ϕ	90 - ϕ
Y-axis	N/A	90	90
Z-axis	90	90	90 - ψ

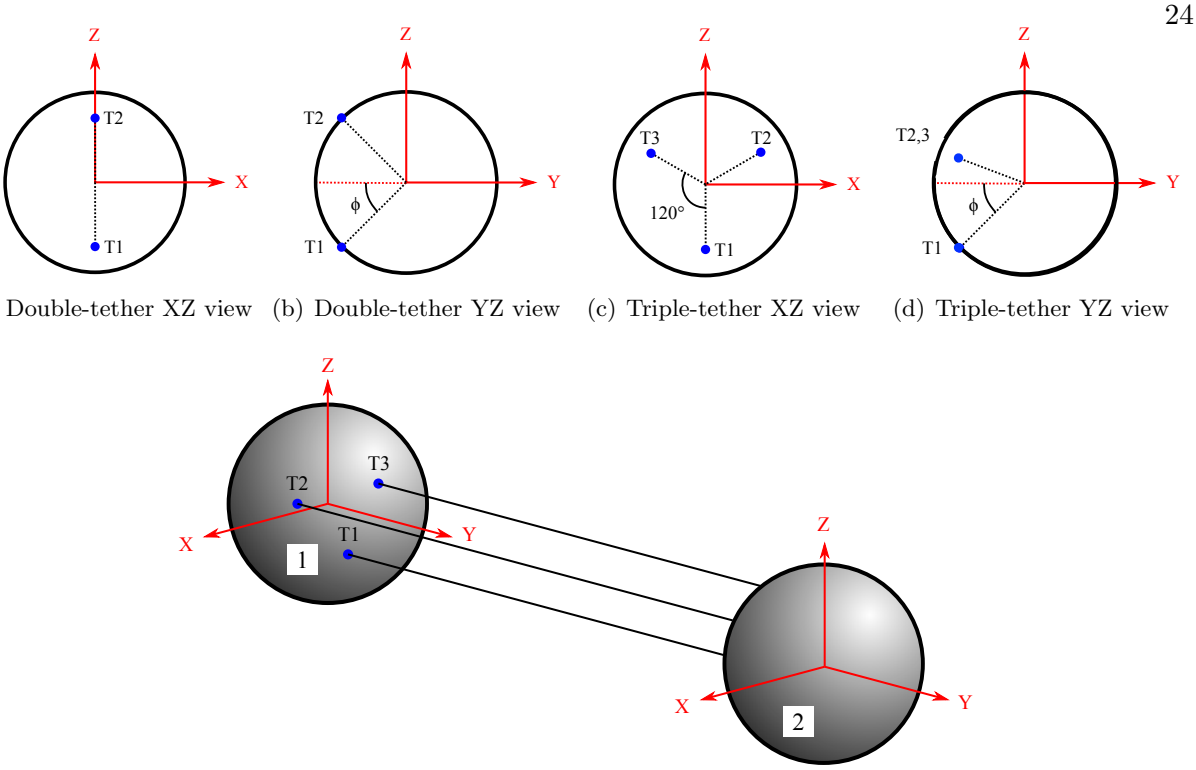

(a) Double-tether XZ view (b) Double-tether YZ view (c) Triple-tether XZ view (d) Triple-tether YZ view

(e) Triple-tether 3D configuration

Figure 4.1: Two-node TCS tether configurations and connections

4.2 Nodal Motion

A single-tether connection yields the simplest and most intuitive dynamics for a two-node TCS configuration under the disturbance of an initial angular velocity. All system properties for the following simulations are identical to those given in Table 3.2 and the tether attachment angle, ϕ, is 45 degrees. Figure 4.2(a) shows the resulting dynamics of the single-tether system under an initial asymmetric nodal rotation about the X-axis. It is important to note that for all results the translational motion is only due to the rotational coupling, as the node is initially at translational equilibrium. Figure 4.2(a) shows the smooth and sinusoidal nodal separation, the asymmetric nodal rotations and the tether tension of a single-tether TCS. Under this small initial rotation disturbance (10 deg/min) the nodes rotate a maximum of 18 degrees about the X-axis and the tether remains under tension at all times. Larger initial disturbances can make the single-tether configuration go

slack and cause the motion to no longer be sinusoidal. In contrast to the single-tether configuration, Figure 4.2(b) shows the translational and rotational motion for the double-tether configuration with initial rotations about the X-axis. The nodal motion is now piecewise linear. The nodes rotate, only about the X-axis, at a constant rate until the tethers become taught and reverse the direction of rotation. The piecewise linearity of a multiple tether TCS is due to the tethers no longer remaining continuously taught. This is shown by the plot of tether tension for each tether (T1 and T2). Maintaining a taught tether is not a required dynamic property, although there is concern of a tether reaching a buckled or tangled state. In these simulations each tether only reaches a slightly loose state on the order of millimeters over its entire 4 meter length.

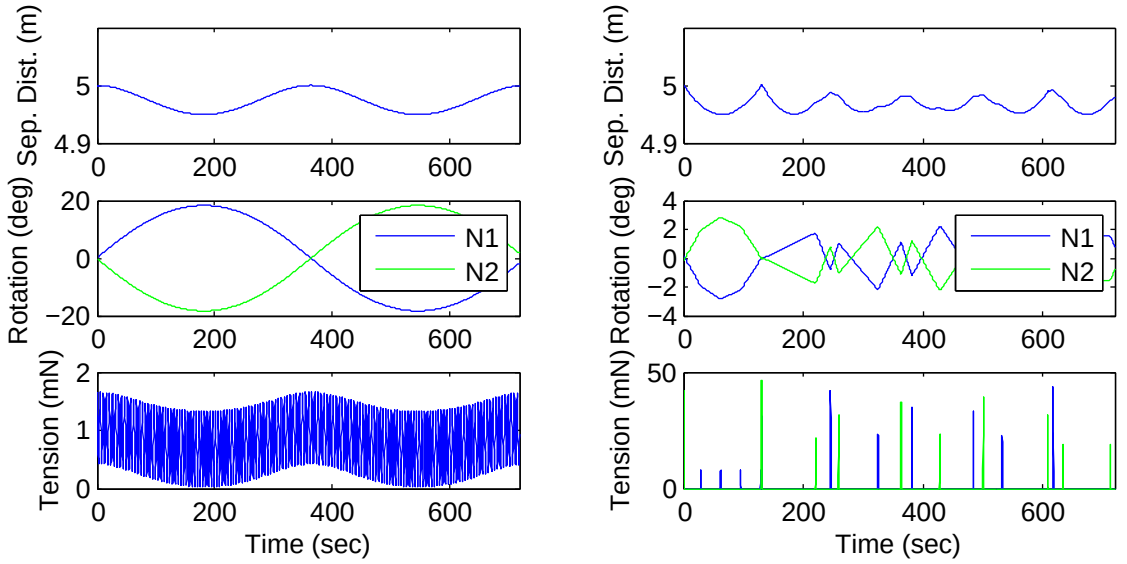

(a) Single-tether configuration

(b) Double-tether configuration

Figure 4.2: TCS nodal dynamic response to asymmetric nodal rotation about the X-axis

The triple-tether configuration results for this X-axis rotation results in similar dynamics to that shown for the double-tether in Figure 4.2(b). Although the triple-tether demonstrates similar separations and X rotations to the double-tether it adds another unique complexity to the two-node TCS configuration. The 3D spread of the triple-tether attachment points adds coupled off-axis rotational motions that is most apparent with rotations about the Z-axis. Figure 4.3 shows the three axes rotational motion of a triple-tether node with an initial rotation about the Z-axis. From the

figure it can be seen that there is no longer pure rotation about the Z-axis. Figures 4.1(c) and 4.1(d) highlight the cause, showing that the connections for tethers 2 and 3 are no longer on a nodal axis and rotation leads to tether force moments and off-axis rotations. Figure 4.3(b) shows the resulting tensions for each tether, reiterating the coupling effect.

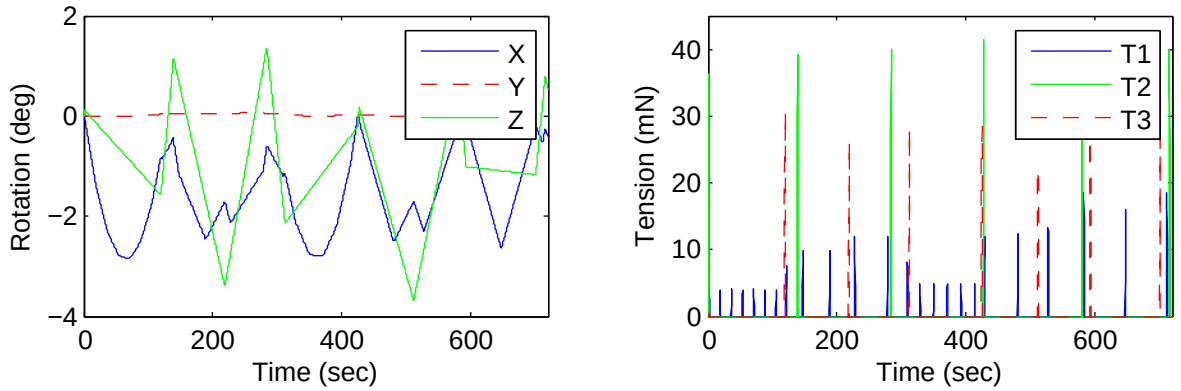

(a) Three axes rotations

(b) Tether tensions

Figure 4.3: Triple-tether nodal dynamic response to asymmetric nodal rotation about the Z-axis

4.3 Multiple Tether Advantages

As shown in the prior sections, additional tethers in a two-node configuration adds complexity to the nodal dynamics. However, there are rotational stiffness advantages that multiple tethers provide. With the inability of a tether to hold torsional loads there is no stiffness in the Y-axis (for a single-tether) and only restoring torques for rotations about the X and Z axes are feasible. Using a TCS configuration with two or three tethers allows for there to be a restoring torque for rotations about any axis.

Additional tethers not only provide added system robustness to initial rotations, but they also reduce the maximum deflection a node can incur. The maximum angular deflection of the node is a measure of the TCS configuration rotational stiffness to an angular rate disturbance. Figure 4.4 demonstrates this by showing the maximum principal rotation angle reached as a function of initial angular rate. The maximum rotation is shown for each of the tether number configurations and

shown for three cases, each with an initial rotation about a different axis. Note the difference in the angular rate axis of each of these figures. Angular rates about the Y-axis result in large rotations much faster than the other two axis rotations. It is shown in Table 4.1 that the multiple tether nodes have a reduced absolute rotation before entanglement occurs. For this reason Figure 4.5 shows the maximum rotation of the nodes relative to their corresponding entanglement rotation angle. Additionally, Figure 4.6 reiterates the effect of multiple tethers on node rotation by showing the absolute maximum rotations as a function of node potential for an initial 10 deg/min rotation. The rotation about each axis is analyzed using the results of Figures 4.4-4.6.

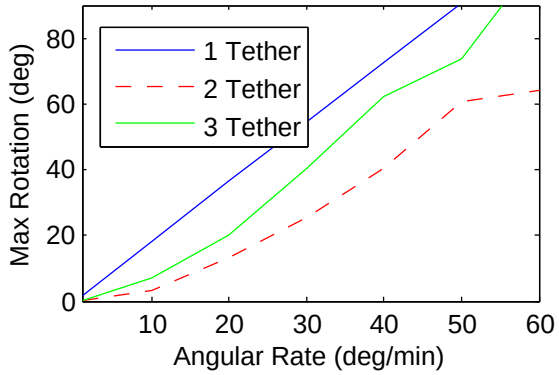

(a) Case 1: X-axis rotation

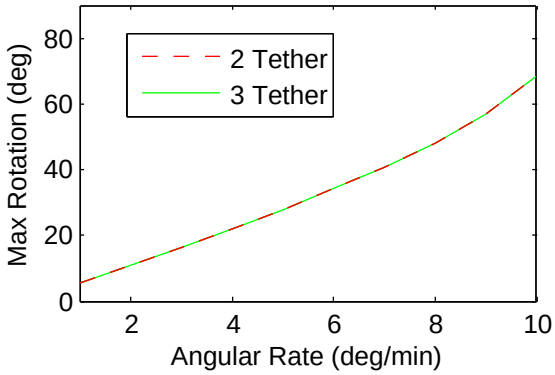

(b) Case 2: Y-axis rotation

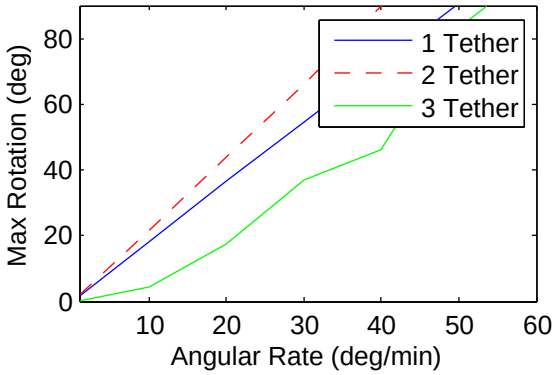

(c) Case 3: Z-axis rotation

Figure 4.4: Maximum absolute principal rotation as a function of initial angular rate

Case 1 X-Axis: Figure 4.4(a) shows that for asymmetric rotation about the X-axis, the addition of tethers reduces the maximum absolute angle reached from the single-tether case. For

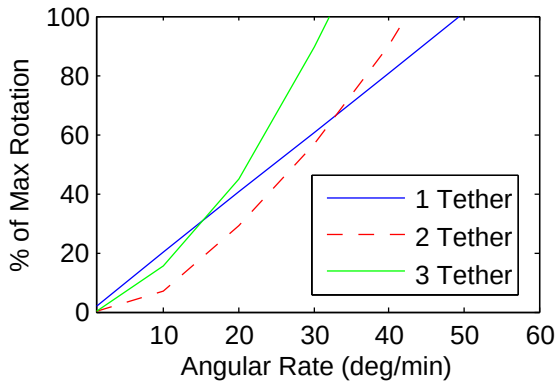

(a) Case 1: X-axis rotation

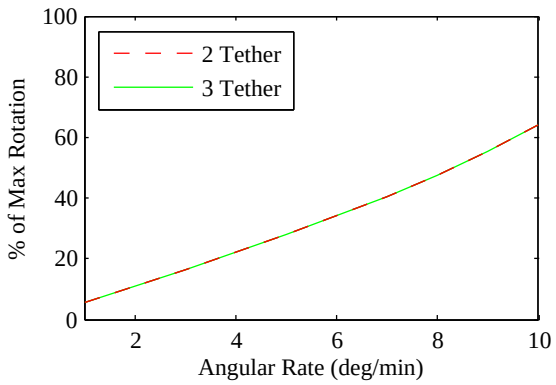

(b) Case 2: Y-axis rotation

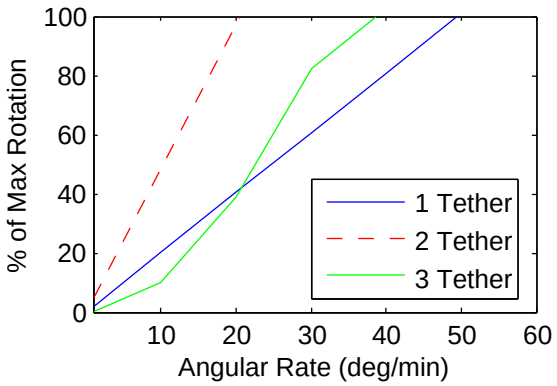

(c) Case 3: Z-axis rotation

Figure 4.5: Maximum principal rotation relative to maximum entanglement rotation (Table 4.1)

lower initial rotation rates, a double- and triple-tether configuration yield similar rotations. At higher rates the double-tether provides more stiffness than the triple-tether This is likely due to the moment arms provided by the tethers. From Figures 4.1(b) and 4.1(d) it can be seen that the attachment points in the positive Z direction for the two tether configuration are further away from the X-axis than the three tether configuration. This difference provides a larger moment arm for the restoring torques and is one reason the double-tether configuration is stiffer at higher rates for this rotation. Additionally at higher rotation rates, the rotation coupling becomes more dominant which increases the maximum rotation rate for a triple-tether configuration.

While the addition of tethers certainly reduces the absolute rotational deflection of the node, the increased tether attachment locations places the node closer to the entanglement rotation. This

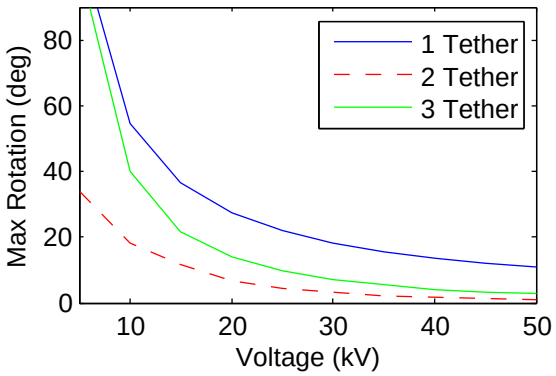

(a) Case 1: X-axis rotation

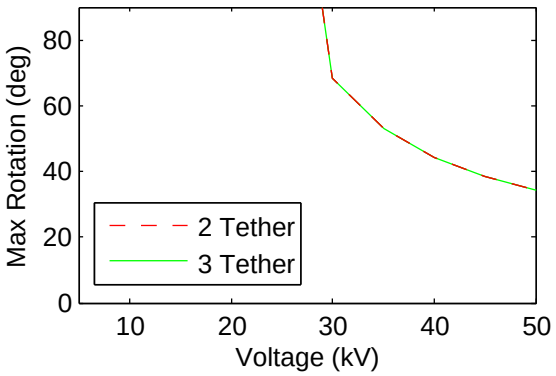

(b) Case 2: Y-axis rotation

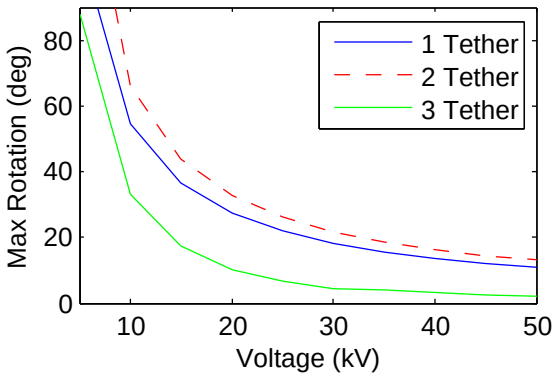

(c) Case 3: Z-axis rotation

Figure 4.6: Maximum absolute principal rotation as a function of nodal potential

is demonstrated in Figure 4.5(a) which shows the maximum angular deflection as a percentage of the entanglement rotation, which is a function of each tether configuration and rotation axis (as defined in Table 4.1). For low initial rotation rates the double-tether keeps the nodes the furthest away from entanglement. Also, for low rotation rates, the triple-tether and single-tether provide similar robustness to entanglement. However, as rates increase the performance of the double- and triple-tether degrade faster than the single. Resulting in the triple-tether reaching an entanglement state at about 30 deg/min and the double-tether reaching entanglement at about 40 deg/min.

The effect of multiple tethers on X-axis rotation as a function of node potential is seen in Figure 4.6(a). The double- and triple-tether both provide more rotational stiffness across all node potentials than a single-tether TCS configuration. The double-tether does provide a slightly

more stiff system than the triple-tether configuration. The non-smooth nature of the triple-tether configuration is due to the complex dynamics of the system, but a general exponential decay can still be seen.

Case 2 Y-Axis: Rotational stiffness about the Y-axis for a double- and triple-tether configuration is shown in Figure 4.4(b). The single-tether configuration is omitted because it has no rotational stiffness for Y-axis rotations. From the Figure it can be seen that the double- and triple-tether configurations provide equal rotational stiffness about the Y-axis, because the moment arms about the Y-axis are equal. Figures 4.1(a) and 4.1(c) show how the moment arms are all the same radial distance from the Y-axis.

Figure 4.5(b) shows how close the Y-axis angular deflection comes to reaching the entanglement angle. The Y-axis has a reduced disturbance angular rate as the nodes have less rotational stiffness, however the inclusion of additional tethers provides prevention of entanglement for the disturbance range analyzed. In this case the single-tether entanglement rotation is undefined as the tether is bound about itself.

Figure 4.6(b) provides additional evidence of the effects of multiple tethers on Y-axis rotation. Again the double- and triple-tether configurations perform identically. However, at lower potentials the nodes reach entanglement and are omitted from the plot. The lower rotation rates and the large node rotation agrees with Figure 4.4(b) and shows that for a two-node TCS configuration the Y-axis has the least rotational stiffness.

Case 3 Z-Axis: For a single-tether TCS, the Z-axis rotation is identical to X-axis rotation. However, Figure 4.4(c) shows that a double-tether configuration provides less stiffness than a single-tether for rotations about the Z-axis. Again the moment arm is the cause for this reduced stiffness. The moment arm about the Z-axis in Figure 4.1(b) is less than what the moment arm of a single-tether provides. The moment arm for this configuration is only in the Y direction and is reduced proportionally to the attachment angle ϕ. A triple-tether configuration also has a moment arm that is dependent on ϕ but the maximum rotation is less than that of a single-tether. The additional stiffness in a three tether configuration is because tethers 2 and 3 in Figure 4.1(d) provide a larger

moment arm about the Z-axis. The larger moment arm arises because tethers 2 and 3 are not located in the ZY plane, which adds additional length to the moment arm.

The relative angular deflection about the Z-axis is shown in Figure 4.5(c). These results indicate that the double-tether system will reach entanglement at disturbances above 20 deg/min. The triple-tether however performs significantly better than than the double- and single-tether configurations at keeping the node away from entanglement for low rotation rates.

The rotational stiffness for rotations about the Z-axis and dependence on node potential is shown in Figure 4.6(c). The figure shows that a triple-tether configuration provides more rotational stiffness than a single-tether. Also, a double-tether configuration again provides lower stiffness than a single-tether for rotations about the Z-axis because of moment arm lengths.

Case Summary: The results of Figure 4.4 indicate that there is up to a 60% decrease in the absolute maximum angular rotation about the X-axis by using a triple-tether over a single-tether. Similarly, there is up to a 35% decrease in the Z-axis rotation with a triple-tether over the single. As the single-tether offers no Y-axis rotational stiffness the addition of tethers does provide rotational stiffness. These values are approximate and are calculated for an initial rotation rate of 30 deg/min and a node voltage of 30 kV. The actual quantitative increase in stiffness is a function of the initial rotation rate and node potential.

The multiple tether configurations have a geometry that places the tether attachment point closer to the entanglement rotation prior to any rotational motion. The results of Figure 4.5 indicate that the multiple tethers offer minimal advantage in reducing the chances of entanglement, and sometimes performs worse than a single-tether. The advantage of using multiple tethers is that it reduces the absolute nodal rotation for an equivalent initial disturbance as well as introducing 3D rotational stiffness. Additionally, the issue of entanglement could be overcome by placing the tethers on booms away from the spherical surface of the spacecraft.

In addition, from these results it would appear that a equally spaced quad tether would offer all axis rotational stiffness as well as symmetric moment arms. This combination may provide an advantageous rotational stiffness capability over the tether configurations used in this study.

However, a quad tether configuration is no longer statically determinate and any slight discrepancy in tether length results in asymmetric motions. This concept is to be investigated in future studies.

4.4 Multiple Tether Nodal Properties

The effects of nodal properties for a single-tether TCS are examined in Section 3.2.2. Similar results for mass and inertia variation can be shown for multi-tether TCS. The results are shifted similarly to those in the previous section. With multi-tether TCS there is one additional nodal property that can affect the rotational stiffness, the tether connection angle, ϕ, shown in Figure 4.1. Figure 4.7 shows the results of a double-and triple-tether TCS configuration as a function of the tether attachment angle ϕ. All other simulation parameters are listed in Table 3.2.

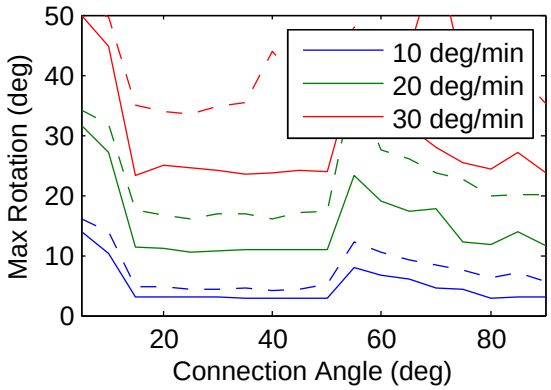

Figure 4.7: Variation in tether attachment angle (solid: double-tether, dashed: triple-tether)

Figure 4.7 shows that as the tether attachment angle increases, the moment arm increases, thus the maximum absolute rotation decreases. Based on the results of this figure an ideal tether attachment angle is approximately between 20 to 45 degrees. A large angle (ϕ) near 90 degrees can provide similar rotation restrictions, but places the node much closer to the tether entanglement rotation, as defined in Table 4.1.

Chapter 5

TCS Perturbations

5.1 Orbital Perturbation Study

The full translational equations of motion, Equation 2.16, for a TCS models a system that is affected by differential gravity and solar radiation pressure (SRP). However, both forces have been neglected in previous sections to isolate effects on translational and rotational motion. This section examines both perturbations separately and provides justification for using the simplified equations of motion of Equation 2.17. A two-node TCS will be used for this analysis. Since the rotational and translational equations of motion are coupled, both the translation and rotation of a two node TCS are investigated.

5.2 Differential Gravity

Previous simulations examine TCS rotational motion with no gravitational effects. However, TCS systems are envisioned to be operated at GEO where differential gravity can affect the nodal dynamics. A two node TCS system will only be stable on orbit if the two nodes are in an orbit radial configuration. This condition is also stable if the nodes undergo initial asymmetric rotations. Table 5.1 shows the percent difference between the max principal rotations of a two-node TCS system with 10 deg/min asymmetric initial rotations in deep space as compared to GEO. From the table it can be seen that putting the benchmark problem into GEO has minimal effect on the rotation of the TCS system. Therefore, differential gravity can be excluded from simple rotational simulations so that the TCS system dynamics can be isolated and analyzed. However, it is impor-

tant to note that with differential gravity effects, rotations are no longer purely about a single axis for single- and double-tether TCS but they are very small respectively.

Table 5.1: Max rotation percent difference between Deep Space and GEO

Initial Rotation Axis	Single-Tether	Double-Tether	Triple-Tether
X-Axis	-0.0839%	0.6780%	-1.1596%
Y-Axis	N/A	-0.1514%	-0.1514%
Z-Axis	1.5793%	1.3376%	-2.2354%

5.3 Solar Radiation Pressure

5.3.1 SRP Compression

Solar radiation pressure is the only other prominent external force for spacecraft at GEO. The force on a spacecraft due to solar radiation pressure is given in Equation 2.15. The worst case SRP compression force for a two spacecraft system is when the two TCS nodes are aligned relative to the sun and one node shields the other from the SRP. This worst case configuration is shown in Figure 5.1.

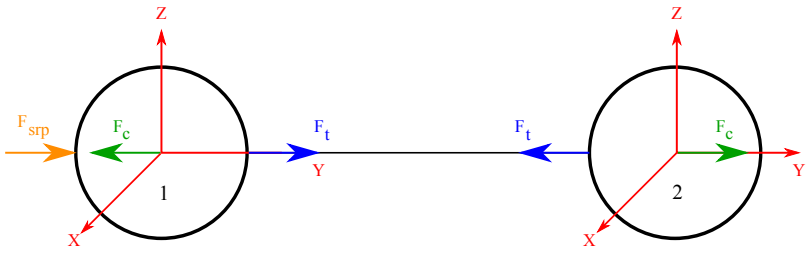

Figure 5.1: Worst case two craft SRP compression configuration

The key concern with SRP and TCS is if it will cause the TCS to lose tension. For the worst case scenario, loss of tension will occur when Coulomb inflationary force between nodes 1 and 2, Equation 2.5, is equal to the SRP force on node 1. Dividing Equation 2.15 by Equation 2.5 yields a percent of lost coulomb force. Simplifying and letting $K = \pi P_{srp} C_r k_c$ be a constant, results in

Table 5.2: SRP rotational simulation parameters

Separation Distance	5 m
Node Mass	50 kg
Spring Constant	35.8398 N/m
Node Charge	30 kV
Node Radius	0.5 m
P_{srp}	4.56e-6 N/m
C_r	1

the percent of lost Coulomb force

$$\%LCF = K\frac{r_{12}^2}{V^2 e^{-(r_{12}-\rho)/\lambda_D}\left(1+\frac{r_{12}}{\lambda_d}\right)}100 \tag{5.1}$$

which only depends on the node voltage(V), separation distance (r_{12}), the node radii (ρ) and the Debye length (λ_d). However, if the nodes are not the same radius, the ratio of the crafts radii must be added to the numerator of Equation 5.1. The simulation is started at TCS equilibrium with the parameters of Table 5.2. As long as the percent of lost coulomb force is less than 100, there will be no loss of tension in the TCS. Figure 5.2 shows the percent of lost Coulomb force for the plausible operating regions for a two identical node craft in deep space.

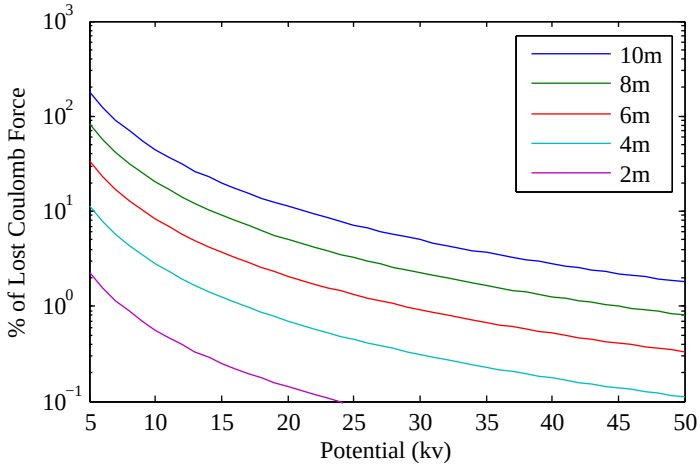

Figure 5.2: Percentage of lost Coulomb force

It is important to note that this is for the worst case configuration with a worst case Debye

length of 4 m. Even so, the SRP force only overcomes the Coulomb force for low potential values at high separation distances. Looking at the typical operating regions of 30 kV potentials and 5 m separation. Figure 5.2 shows that the SRP force is less than a percent of the Coulomb force and thus can be considered negligible.

Note that this plot shows this force ratio percentage on a logarithmic scale. For the voltages (20-40kV) and separation distances (2-5m) that are being considered between the nodes, the solar radiation force is 2-3 orders of magnitude smaller than the Coulomb force. For smaller TCS configurations the solar radiation pressure will have a negligible impact. However, as larger TCS node clusters are considered, the differential solar could contribute to large scale flexing of the TCS shape.

5.3.2 SRP Torques

The effects of solar radiation pressure on TCS compression is not the only way SRP can affect a TCS. SRP may also induce torques on a TCS. Two different worst case SRP torque scenarios are examined for a single tether two node TCS in deep space. The first scenario is a SRP torque about the system center of mass. This can arise when one craft is experiencing the effects of SRP and the other is not, due do some external shielding of a craft. The SRP torque about the center of mass scenario is shown in Figure 5.3.

Assuming the two craft are identical and that the SRP force is given in Equation 2.15, then the torque on the system will be given by

$$T_{srp} = F_{srp}\frac{r}{2} \tag{5.2}$$

where r is the node separation distance. Since this scenario is considered a worst case it is not envisioned to last for long durations. A three hour simulation for the SRP center of mass torque was conducted to examine the effects of the torque. The simulation was started with the Coulomb and tensile forces in equilibrium. The parameters for the simulation are shown in Table 5.2. The simulation shows that as expected, the two craft TCS begins to rotate about its center of mass due

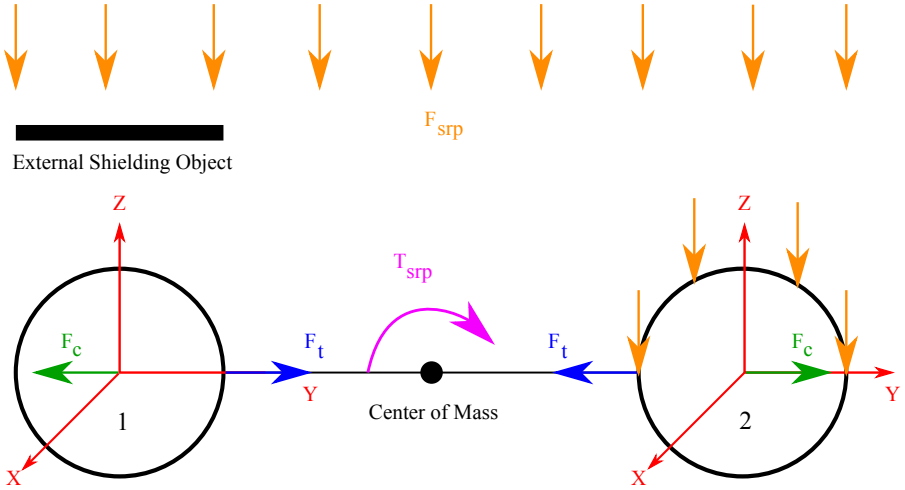

Figure 5.3: SRP center of mass torque scenario

to the external torque. After the three hour simulation the TCS was rotating at 1.5e-4 rad/s about the center of mass. However, when working with formations of spacecraft the relative positions and rotations are often of more importance. The change in relative position and rotation for the simulation was less than 1e-15 m and 1e-15 deg, effectively zero. Therefore the only concern with having a SRP torque around the system center of mass is that the system will begin to rotate as a whole.

The second SRP torque of interest is an SRP body torque. This type of torque can occur if a only a portion of a spacecraft is shielded. Figure 5.4 show a possible scenario. The figure shows that node one shields approximately half of node two from the SRP force. Therefore the SRP force on node two is given by

$$F_{srp_2} = P_{srp} C_r \frac{A_{sc}}{2} \tag{5.3}$$

This force is simplified by by assuming the SRP only acts on a half sphere instead of the crescent shape that most likely would occur with spherical craft. This total force is applied at the centroid of the cross-section half-circle of node two and results in the body torque

$$T_{srp} = F_{srp} \frac{4r}{3\pi} \tag{5.4}$$

where r is the radius of the node. This type of SRP torque, one that arises when nodes shield

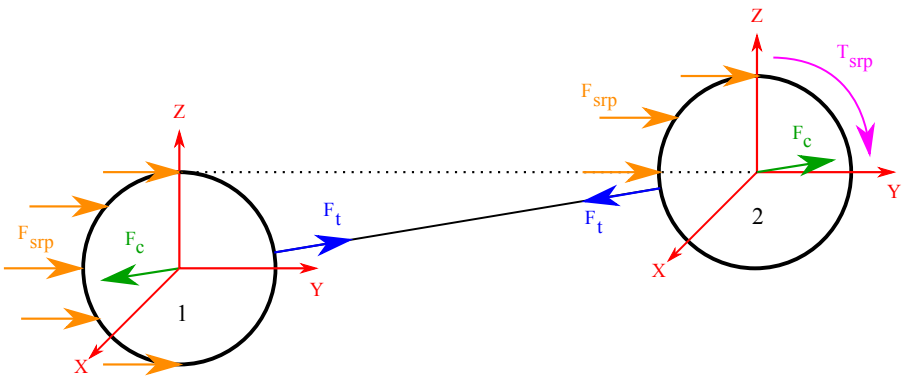

Figure 5.4: SRP body torque scenario

other nodes, will become more prominent when working with larger TCS systems that have many nodes. A simulation is run where the only SRP force applied is on half of node two. The force on node one is neglected to isolate the effects of the body torque on one node. The nodes are started at equilibrium and all parameters are listed in Table 5.2. The change in relative position between the two nodes is again less than 1e-15 m. However, there is a change in relative rotation, which is shown in Figure 5.5. From the figure it can be seen that there is max relative rotation of 0.1 deg

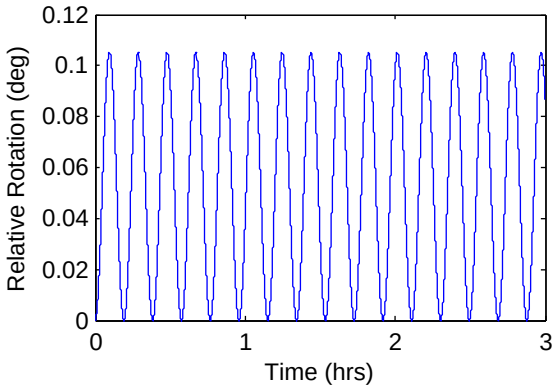

Figure 5.5: SRP body torque relative rotation

between the two craft. The rotation due to SRP body torques is minimal and the effects of these torque will not be the dominating perturbation.

The results of both SRP induced torque scenarios show that SRP will only have minimal effects on a TCS. The relative positions and rotation between TCS will be negligibly affected. The

key effect from solar radiation pressure is that it will rotate a TCS system as a whole. This, like most other space systems affected by SRP, could be counteracted using thrusters or momentum wheels.

Chapter 6

Mother Child TCS

6.1 Mother Child Set-Up

One envisioned use of a TCS is to provide local situational awareness for a geosynchronous satellite. Here one large spacecraft (the Mother) has a smaller spacecraft (the Child) tethered to it as illustrated in Figure 6.1. This type of TCS configuration can provide a unique vantage point for on-orbit inspection of the Mother craft, rendezvous, docking and refueling operations and space environment measurements. The key advantage that a TCS can provide for situational awareness at GEO is that it can hold a Child spacecraft at a relatively fixed position and angle with respect to the Mother craft with minimal use of control and propulsion.

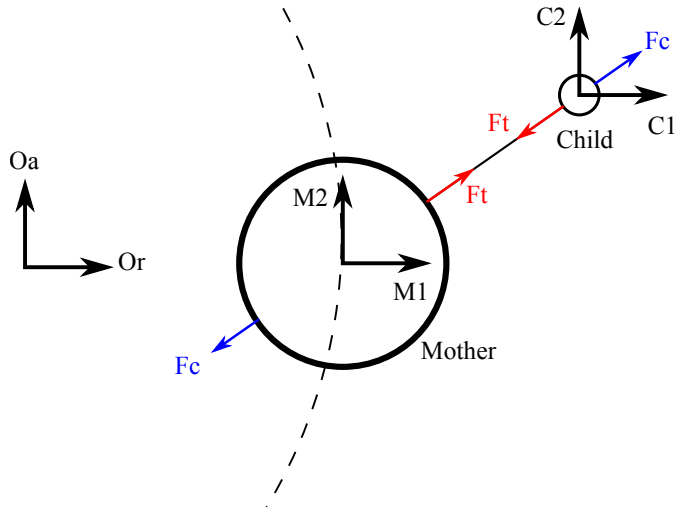

Figure 6.1: Illustration of Mother Child spacecraft scenario

6.2 TCS vs Tethered Structure

The trivial set up for a Mother Child TCS configuration is when the two craft are in the orbit radial configuration. This type of system would even be effective for spacecraft without charge, but less robust to perturbations. Charging the spacecraft allows for additional configurations with negligible relative translation and rotation. For example, using the parameters in Table 6.1, the maximum relative translation and rotation of the two craft after one orbit when the craft are oriented in either of the principal local vertical local horizontal directions is less than 1 mm and 0.001 deg, respectively. These simulations use a one tether TCS where the spacecraft started with initial Coulomb and tensile forces in equilibrium. Additionally, the craft have rotation rates equal to that of the orbit frame (360 deg/day).

Table 6.1: Mother Child simulation parameters

Parameters	Mother	Child
Mass (kg)	2000	50
Radius (m)	2	0.5
Voltage (kV)	30	30
Separation (m)	7	7

A configuration of more interest is when the Child craft is placed at an arbitrary position relative to the mother craft. One such example would be placing the Child craft where it would have positive radial and along track components relative to the Mother craft. Figure 6.2 shows time elapsed snapshots of a tethered structure (TS) and TCS for this set up with the system parameters given in Table 6.1. From the figure it can be seen that for a TS the relative position and attitude of the two craft varies over an orbit. The tether is mostly slack and the child craft only rotates the Mother craft after approximately 5 hours. The TCS however, maintains a reasonably fixed relative position and rotation between the two craft and the changes in relative position and rotation from the initial conditions can be seen in Figure 6.3. The reason for this consistency is that the tether between the two craft remains almost always in tension throughout the orbit. These results are

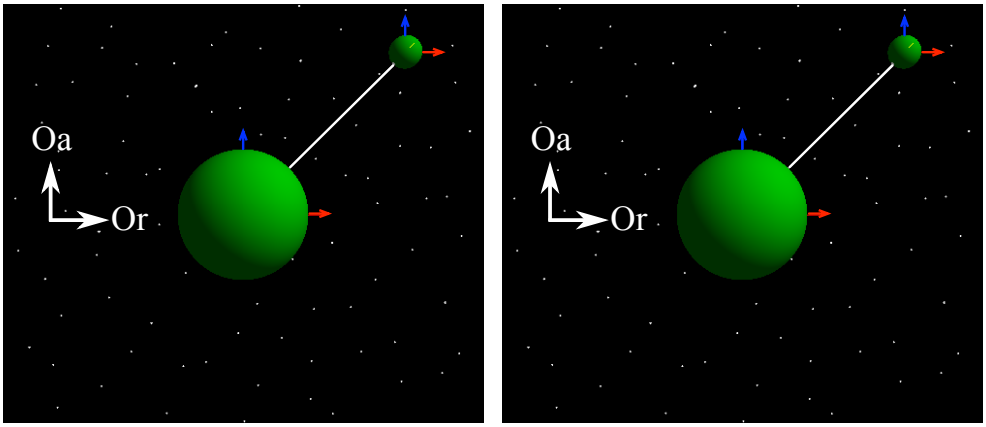

(a) TS at t = 0 hrs (b) TCS at t = 0 hrs

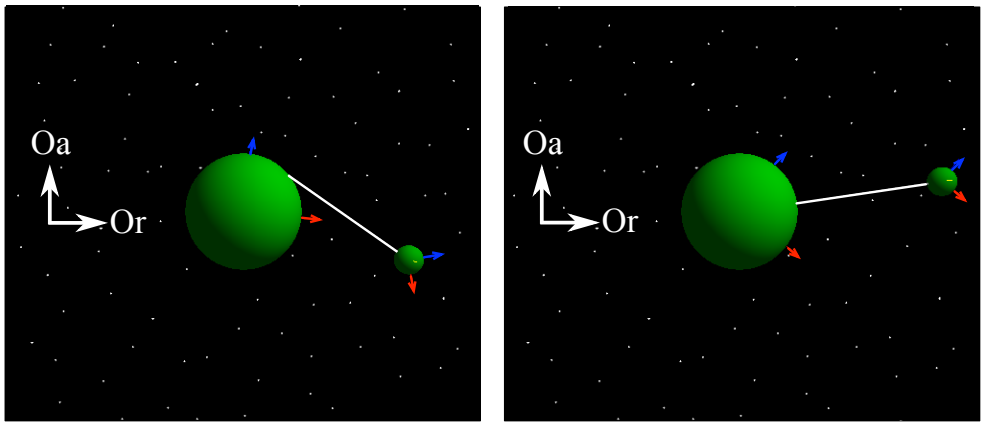

(c) TS at t = 5.5 hrs (d) TCS at t = 5.5 hrs

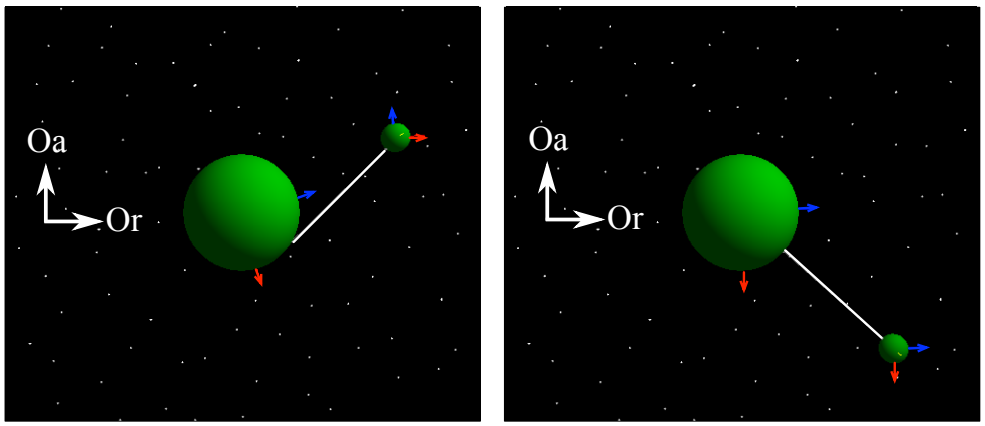

(e) TS at t = 14 hrs (f) TCS at t = 14 hrs

Figure 6.2: TS and TCS comparison of mother child configuration

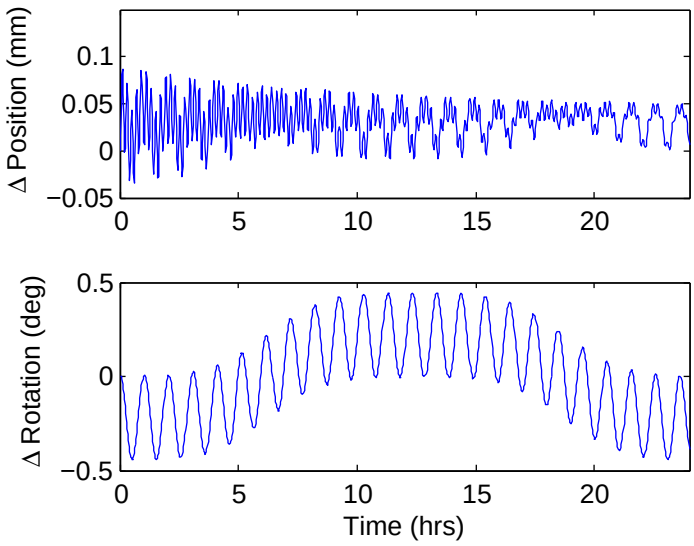

Figure 6.3: TCS Mother Child relative position and rotation

also typical if the Child craft has an out of plane component, relative to the Mother craft.

6.3 Fixed Mother Craft

Even though a Mother Child TCS keeps relative positions and rotations nearly constant for an arbitrary set up, it does cause the system as a whole to rotate relative to the orbit frame. This is typically not desired, but can be easily fixed by implementing a simple attitude control solution. Figure 6.4 shows the relative values for a Mother Child configuration with a stable attitude control given in Equation 6.1 where $[A]$ and $[B]$ are positive definite gain matrices.[19]

$$\boldsymbol{u} = -[A]\boldsymbol{\sigma} - [B]\boldsymbol{\omega} \tag{6.1}$$

In this scenario the Mother craft orientation is held fixed by using high gains, while the tethered Child spacecraft is free to translate and rotate due to the differential gravity and Coulomb forces. Of interest is how much the Child spacecraft will move relative to the Mother craft in this scenario. The parameters for this simulation are given in Table 6.1 and the control was updated at 1Hz with gains of 100.

From Figure 6.4(a) it can be seen that the Child craft position attempts to move in the

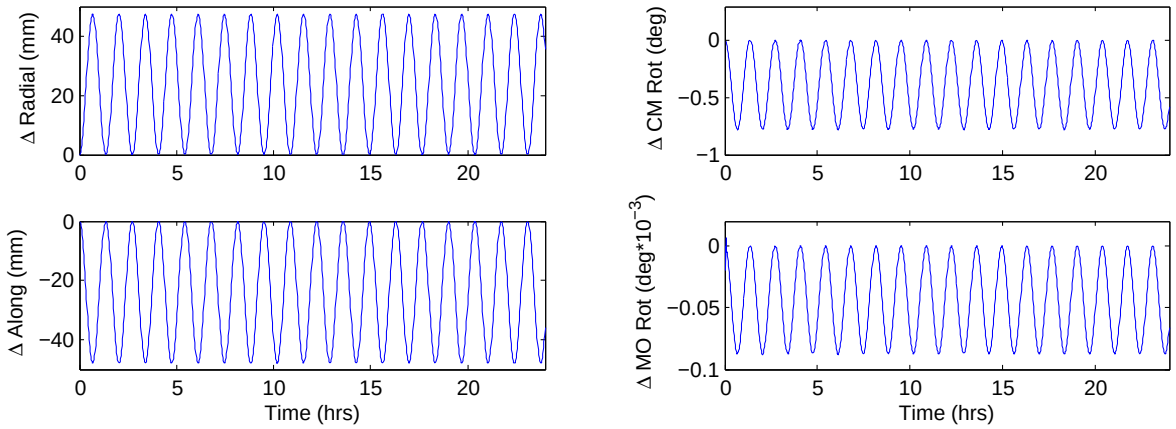

(a) Relative change in position

(b) Child/mother & mother/orbit relative change in rotations

Figure 6.4: TCS Mother Child relative position and rotation with control

positive radial and negative along track position, which is expected for a craft with an initially larger orbit. However, this motion is restricted by the tether and oscillates under 50 mm in each direction. The top plot in Figure 6.4(b) shows the relative rotation between the Child and Mother craft, while the bottom plot illustrates the rotation of the Mother craft relative to the orbit frame. From the figure it can be seen that this simple control can hold a Child craft's orientation within a degree of the Mother and keep the Mother aligned with the orbit frame. The relative motion is larger, as expected, than with the free-mother craft scenario. However, in this constrained Mother craft orientation scenario the relative motions are still held very small with the constant electrostatic force. Additionally, simulations show that out of plane motion can also be constrained with this control law. Since this simple control can constrain the motion of the Child craft it is now beneficial to examine what effects various system parameters have on the configuration's relative dynamics and required torques to determine feasible operating regimes.

6.4 System Parameter Effects

The results from the previous section show that a Mother Child TCS can be controlled and maintained in a relatively fixed position. This section analyzes the effects of system parameters

on the relative positions and rotations as well as the required control torque. The parameters of interest are the separation distance, node voltage and the Child mass. All parameters, except the one being varied, for the following simulations are listed in Table 6.1 and the control from Equation 6.1 is updated at 1Hz with gains of 100. This work addresses the worst case scenario for the Mother Child configuration. Therefore, the Child will be placed equally in the radial, along and cross track directions. Additionally, for reasons similar to those in Chapter 4 multiple tethers between the two craft will be examined.

6.4.1 Separation Distance

The distance between the Mother and Child craft determines what operations the child can perform, as well as what field of view the Child will have of the Mother. The larger the separation distance between the two, the greater field of view the Child will have of the Mother for inspections and situational awareness. Figure 6.5 shows the max relative rotations, max variation in separation distance and required torques for various Mother Child separation distances. All three plots in Figure 6.5 show that increasing separation distance increases the maximum relative rotation, the maximum variation of relative distance and the required torque. Figures 6.5(a) & 6.5(b) show that Mother Child TCS have reduced rotations and variations in separation distance with increasing tether number. This reduced rotation result agrees with that of Chapter 4. Figure 6.5(a) shows that, depending on the Child's task, separation distances of up to 10 m could provide reasonable relative rotations of about five degrees for this worse case scenario. The results of Figure 6.5(b) show that there will only be sub centimeter variations in separation distance between the two craft for all separation distances analyzed. Lastly, Figure 6.5(c) shows that using multiple tethers has negligible effects on the required torque.

6.4.2 Node Voltage

Voltage of the Mother and Child spacecrafts determines what the magnitude of the repulsion force between the two spacecraft is. From a spacecraft design perspective, the lower the voltage

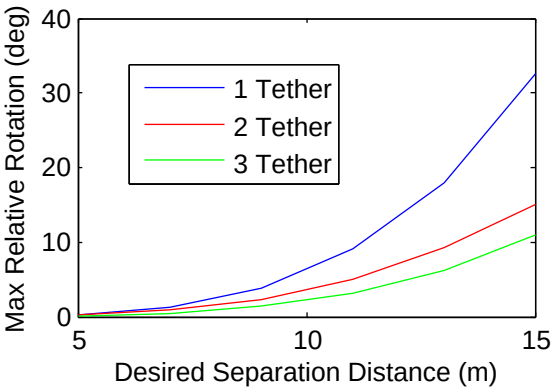

(a) Max Relative Rotation

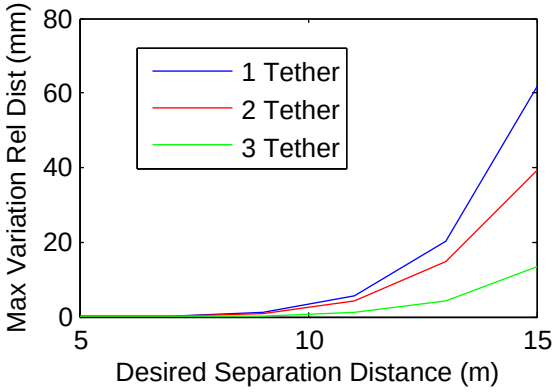

(b) Max Distance Variation

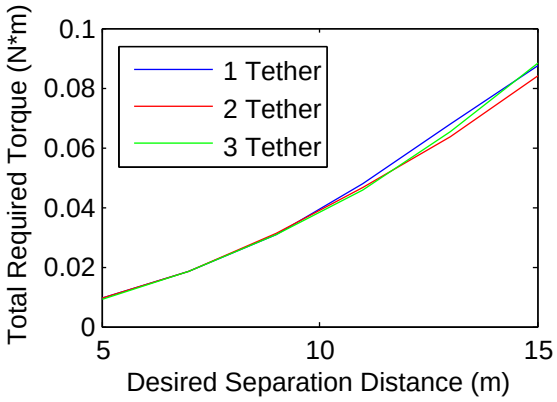

(c) Required Control Torque

Figure 6.5: Mother Child separation distance variation effects

required on the craft the better. For these simulations there is an identical voltage on each craft, but in practice different voltages could be used to simplify the design of either craft. Figure 6.6 shows the relative rotations, max variation is separation distance and required torques for various Mother Child voltages. Similar to the distance variation, Figures 6.6(a) & 6.6(b) show that addition of tethers decreases the maximum relative rotations and distance variations. Additionally, these figures show that increasing voltages also decreases these relative quantities. However, from Figure 6.6(c) it can be seen that neither additional tethers nor increasing voltage has an effect on the required torque to maintain the shape configuration. This is expected because torque is dependent on the transverse force and the moment arm. Even so, this shows that the rigidity of the connection between the Mother and Child has no effect on the required control torque.

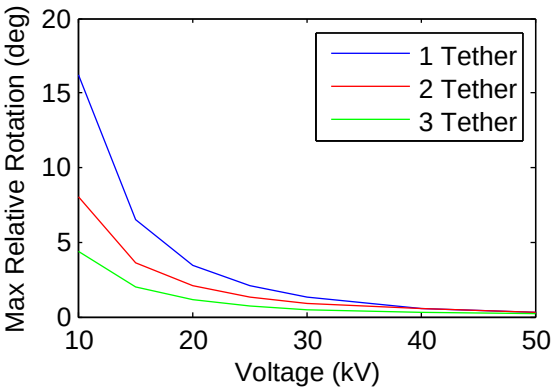

(a) Max Relative Rotation

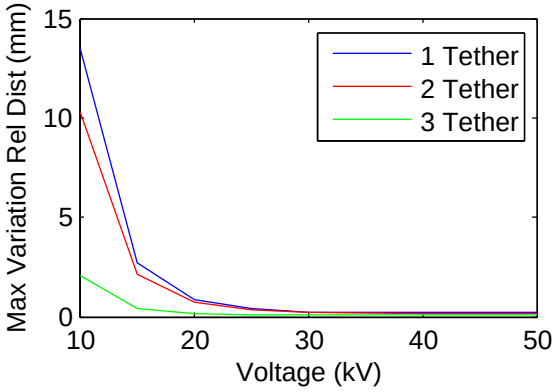

(b) Max Distance Variation

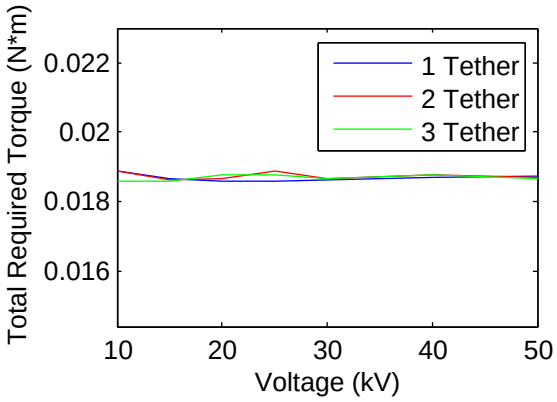

(c) Required Control Torque

Figure 6.6: Mother Child voltage variation effects

6.4.3 Node Mass

The mass of the Child craft will likely depend on its function and that function's required hardware. This section analyzes the effects of various masses on the dynamics of the Mother Child TCS. Figure 6.7 shows the relative rotations, max variation is separation distance and required torques for various Child masses. The data in Figures 6.7(a), 6.7(b) & 6.7(b) show that lower mass nodes minimize the relative dynamics of the Mother child configuration as well as minimizes the required control torque. Figures 6.7(a) & 6.7(b) show that additional tethers provide increased stiffness off a Mother Child TCS. However, similar to previous sections, multiple tethers have no effect on the required control.

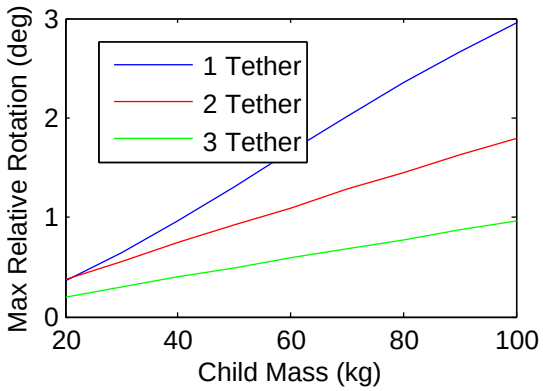

(a) Max Relative Rotation

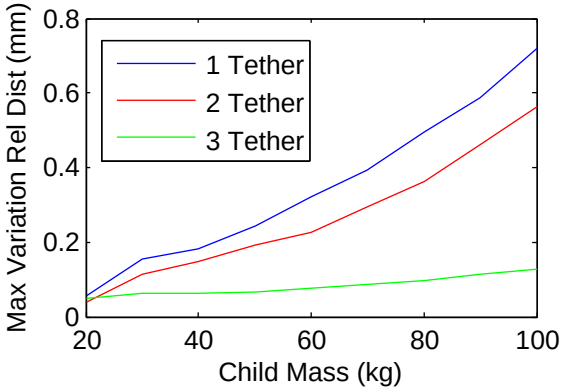

(b) Max Distance Variation

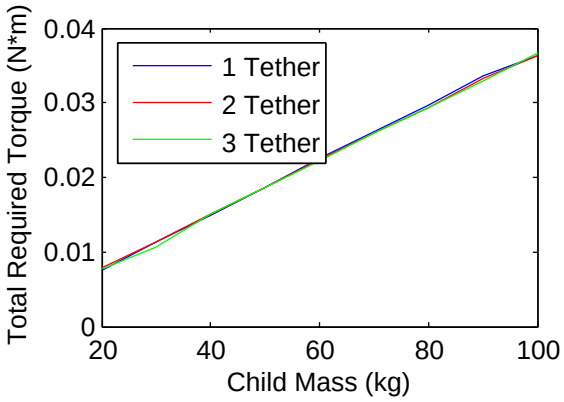

(c) Required Control Torque

Figure 6.7: Mother Child mass variation effects

6.5 Mother Child Summary

Having a relatively close on-orbit point of reference for a large GEO spacecraft provides many unique opportunities for that craft. Holding a spacecraft at a arbitrary and relatively fixed position relative to a larger craft can not be accomplished with a simple tethered spacecraft. However, the analysis of the Mother Child TCS concept shows that with a simple control, (Equation 6.1) a TCS can hold a smaller Child craft relatively fixed at any desired position while in orbit. Further analysis shows that separation distances of up to 10m results in minimal relative rotation (¡ 5 degree) and variations in separation distance (¡ 1 cm). The required control torque is also less than 0.04 Nm per orbit. Optimal Mother Child configurations with the most stiffness occur with low separation distance, high voltage and low Child mass. Lastly, it is shown that multiple tethers between the

craft can greatly increase the stiffness of a Mother Child TCS and allow for separation distances of up to 15 m, depending on the child's function.

Chapter 7

Conclusions and Future Work

This work examines the dynamics of TCS systems. Force models and equations of motion are given. Simulations are conducted to examine the effects of varying system parameters on translational and rotational stiffness for a two node TCS. It is found that systems with nodes that have low mass, high potential and that are close together provide the highest translational and rotational stiffness. Additionally, it is shown that tether properties have negligible effects on rotational motion.

Rotational analysis of a single tether two-node TCS configuration with 30 kV potentials and a 5 m separation shows that this configuration can withstand moderate initial rotations up to around 50 deg/min before the tether would become entangle with the spacecraft. Also, adding additional tethers yields full three-dimensional stiffness and increases the maximum allowable initial rotation by 40-60%. However, tether entanglement will now occur at lower absolute values of rotation, if the nodes are spherical. Finally, for optimal rotational stiffness it is found that the ideal node configuration should have most of its mass at the center of the structure with the largest possible radius for the tether attachment points and if multiple tethers are used, the optimal connection angle is 45 degrees.

The effects of orbital perturbations caused by differential gravity and solar radiation pressure are analyzed. Simulations show that differential gravity has minimal effect on the rotations of the two-node benchmark TCS. Compression of a TCS system due to solar radiation pressure can be considered negligible because it only has noticeable effects for low potentials (¡10 kV) and large

separation distances (¿ 10 m). Nodal torques due to SRP show that only when there is partial shielding of a node will the torques affect relative position and rotation of TCS. However, SRP can cause TCS systems to rotate as a whole.

Lastly, the Mother Child TCS concept is presented to show a practical TCS use. Mother Child simulations show that a TCS can be used to hold a small craft relatively fixed to a large craft in any orbit configuration if an attitude controller is implemented on the Mother craft. Relative rotations and translations between the Mother and Child spacecraft can be limited to less than 5 degrees and 10cm for a 10 meter separation between spacecraft in a worst case orbit configuration. The Mother Child stiffness can be increased by using lower separation distances, higher voltages and lower mass Child nodes. Additionally, more favorable orbit configurations, no cross track separation, can greatly increase the Mother Child stiffness.

Future work for the TCS dynamics studies could be to study the use of more than two spacecraft for full three-dimensional stiffness. Controlled deployment of a TCS is also an aspect of TCS systems that needs to be addressed. Lastly, control laws for damping of a TCS system should be examined as well as other methods of system stabilization.

Bibliography

[1] Gary Blackwood, Curt Henry, Eugene Serabyn, Serge Dubovitsky, MiMi Aung, and Steven M. Gunter. Technology and design of an infrared interferometer for the terrestrial planet finder. In AIAA Space 2003, Long Beach, CA, Sept. 23–25 2003. Paper No. AIAA 2003-6329.

[2] Owen Brown and Paul Eremenko. Fractionated space architectures: A vision for responsive space. In 4th Responsive Space Conference, Los Angeles, CA, April 23–26 2006. Paper No. AIAA-RS-2006-1002.

[3] Kenneth G. Carpenter, Carolus J. Schrijver, Margarita Karovska, and SI Mission Concet Development Team. The stellar imager (si) project: A deep space uv/optical interferometer (uvoi) to observe the universe at 0.1 milli-arcsec angular resolution. Astrophysics and Space Science, 320(1-3):217–223, April 2009.

[4] J. F. Fennell, H. C. Koons, J. L. Roeder, and J. B. Blake. Spacecraft charging: Observations and relationship to satellite anomalies. In Proceedings of 7th Spacecraft Charging Technology Conference, pages 279–285, Noordwijk, The Netherlands, April 23–27 2001. ESA Spec. Publ.

[5] Henry B. Garrett and Albert C. Whittlesey. Spacecraft charging, an update. IEEE Transactions on Plasma Science, 28(6):2017–2028, Dec. 2000.

[6] Jessica Gersh. Architecting the very-large-aperture flux-pinned space telescope: A scalable, modular obtical array with high agility and passively stable orbital dynamics. In AAS/AIAA Astrodynamics Specialist Conference, Honolulu, Hawaii, Aug. 18–21 2008.

[7] D. A Gurnett and Bhattacharjee A. Introduction to Plasma Physics - with Space and Laboratory Applications. Cambridge University Press, New York, NY, 2005. Pages 8–9.

[8] Roderick Hyde. Eyeglass large aperture, lightweight space optics. Technical Report UCRL-ID-151390, University of California, Lawrence Livermore National Laboratory, Feb. 10 2003.

[9] Roderick Hyde, Shamasundar Dixit, Andrew Weisberg, and Michael Rushford. Eyeglass: A very large aperture diffractive space telescope. In Highly Innovative Space Telescope Concepts, 2002.

[10] Dario Izzo and Lorenzo Pettazzi. Self-assembly of large structures in space using intersatellite coulomb forces. In 57th International Astronautical Congress, Valencia, Spain, October 2006. Paper IAC-06-C3.4/D3.4.07.

[11] Lyon B. King, Gordon G. Parker, Satwik Deshmukh, and Jer-Hong Chong. Spacecraft formation-flying using inter-vehicle coulomb forces. Technical report, NASA Institute for Advanced Concepts (NIAC), January 2002.

[12] David W. Miller, , Raymond J. Sedwick, Edmund M. C. Kong, and Samuel Schweighart. Electromagnetic formation flight for sparse aperture telescopes. In IEEE Aerospace Conference Proceedings – Volume 2, Big Sky, Montana, March 9–16 2002.

[13] E.G. Mullen, A. R. Frederickson, G. P. Murphy, K. P. Ray, E. G. Holeman, D.E. Delorey, R. Robson, and M. Farar. An autonomous charge control system at geosynchronous altitude: Flight results for spacecraft design considerations. IEEE Transactions on Nuclear Science, 44(6):2188 – 2914, December 1997.

[14] Naomi Murdoch, Dario Izzo, Claudio Bombardelli, Ian Carnelli, Alain Hilgers, and David Rodgers. Electrostatic tractor for near earth object deflection. In 59th International Astronautical Congress, Glasgow, Scotland, 2008. Paper IAC-08-A3.I.5.

[15] Arun Natarajan and Hanspeter Schaub. Linear dynamics and stability analysis of a coulomb tether formation. AIAA Journal of Guidance, Control, and Dynamics, 29(4):831–839, July–Aug. 2006.

[16] Arun Natarajan and Hanspeter Schaub. Orbit-nadir aligned coulomb tether reconfiguration analysis. In AAS/AIAA Spaceflight Mechanics Meeting, Galveston, TX, Jan. 27–31 2008. Paper AAS 08–149.

[17] Arun Natarajan, Hanspeter Schaub, and Gordon G. Parker. Reconfiguration of a nadir-pointing 2-craft coulomb tether. Journal of British Interplanetary Society, 60(6):209–218, June 2007.

[18] M. A. Peck, B. Streetman, C. M. Saaj, and V. Lappas. Spacecraft formation flying using lorentz forces. Journal of British Interplanetary Society, 60:263–267, July 2007.

[19] Hanspeter Schaub and John L. Junkins. Analytical Mechanics of Space Systems. AIAA Education Series, Reston, VA, 2nd edition, October 2009.

[20] Hanspeter Schaub, Gordon G. Parker, and Lyon B. King. Challenges and prospect of coulomb formations. Journal of the Astronautical Sciences, 52(1–2):169–193, Jan.–June 2004.

[21] Hanspeter Schaub, Gordon G. Parker, and Lyon B. King. Coulomb thrusting application study. Technical report, Virginia Tech and Aerophysics, Jan. 2006.

[22] Carl R. Seubert and Hanspeter Schaub. Tethered coulomb structures: Prospects and challenges. In AAS F. Landis Markley Astrodynamics Symposium, Cambridge, MA, June 30 – July 2 2008. Paper No. AAS 08–269.

[23] Carl R. Seubert and Hanspeter Schaub. Electrostatic force model for terrestrial experiments on the coulomb testbed. In 61st International Astronautical Congress, Prague, CZ, Sept. 2010. International Astronautical Federation. Paper IAC-10.C1.1.9.

[24] Carl R. Seubert and Hanspeter Schaub. Impact of nodal attitude motion on two-element tethered coulomb structures. In AAS/AIAA Spaceflight Mechanics Meeting, San Diego, CA, Feb. 14-17 2010. Paper No. AAS 10–268.

[25] J. Sliško and R.A. Brito-Orta. On approximate formulas for the electrostatic force between two conducting spheres. American Journal of Physics, 66(4):352–355, April 1998.

[26] W. R. Smythe. Static and Dynamic Electricity. McGraw-Hill, 3rd edition, 1968.

[27] K. Torkar, W. Riedler, C. P. Escoubet, M. Fehringer, R. Schmidt, Grard R. J. L., H. Arends, F. Rudenauer, W. Steiger, B. T. Narheim, K. Svenes, R. Torbert, Andre M., A. Fazakerley, R. Goldstein, R. C. Olsen, A. Pedersen, E. Whipple, and H. Zhao. Active spacecraft potential control for cluster – implementation and first results. Annales Geophysicae, 19(10/12):1289–1302, 2001.

[28] K. Torkar, W. Riedler, F. Rudenauer, C. P. Escoubet, H. Arends, B. T. Narheim, K. Svenes, M. P. McCarthy, G. K. Parks, R. P. Lin, and H. Reme. Spacecraft potential control aboard equator-s as a test for cluster-ii. Annales Geophysicae, 17(12):1582–1591, 1999.

[29] Shuquan Wang and Hanspeter Schaub. Switched lyapunov function based coulomb control of a triangular 3-vehicle cluster. In AAS/AIAA Astrodynamics Specialist Conference, Pittsburgh, PA, Aug. 9–13 2009.

[30] Elden C Whipple. Potentials of surfaces in space. Reports on Progress in Physics, 44(11):1197–1250, 1981.

Appendix A

Simulation Validation

A.1 Linearized Equations of Motion

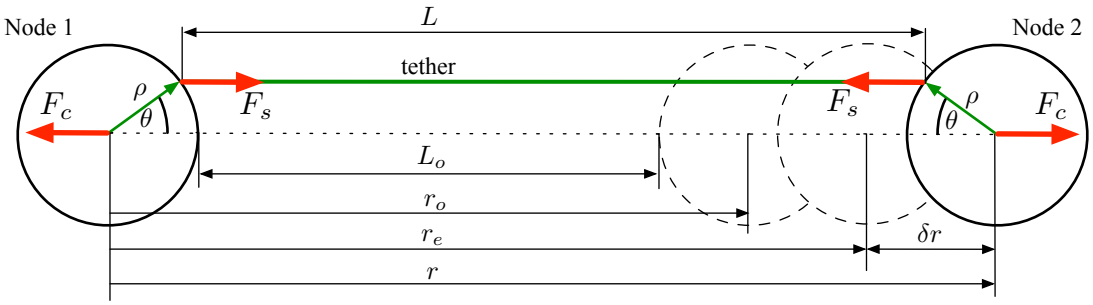

Figure A.1: Asymmetric two-node system with two degrees of freedom

Figure A.1 shows the two-node single tether TCS setup which is the base configuration for the TCS studies in this work. This appendix outlines the verification of the numerical simulation used. The linearized equations of motion for two-node TCS are[23]

$$\delta\ddot{r} \approx -\frac{1}{m}\left[\frac{2k_cQ}{r_e^3(Q)} + k_s\right]\delta x \tag{A.1}$$

for translation and

$$\ddot{\theta} \approx \frac{-\rho k_s}{I}\left[r_e(Q) - r_o\right]\theta \tag{A.2}$$

for rotation where $r_e(Q)$ is the equilibrium separation distance, r_o is the TCS separation distance with no tension in the tether, Q is the charge product of the two nodes. Figure A.1 depicts the two-node TCS these equations are derived for. The linearized equations of motion yield a translational

frequency of

$$\omega_T = \sqrt{\frac{1}{m}\left[\frac{2k_c Q}{r_e^3(Q)} + k_s\right]} \tag{A.3}$$

and a rotational frequency of

$$\omega_R = \sqrt{\frac{\rho k_s}{I}\left[r_e(Q) - r_o\right]} \tag{A.4}$$

Figure A.2 shows a comparison of the TCS simulation translational and rotational frequencies as compared to the analytical frequencies. For the translational frequencies, the TCS was set with each node offset from equilibrium by an equal distance. For the rotational case, the nodes were set at TCS equilibrium and then given an initial rotation. Figure A.2 shows that both translational and rotation frequencies agree with the analytics for small disturbances. However, it can be seen that the linearization begins to break down at a translational offset of more than 10^{-4}m and an initial rotation of more that 1 deg/min. Even so, the figure further validates the use of the numerical simulation.

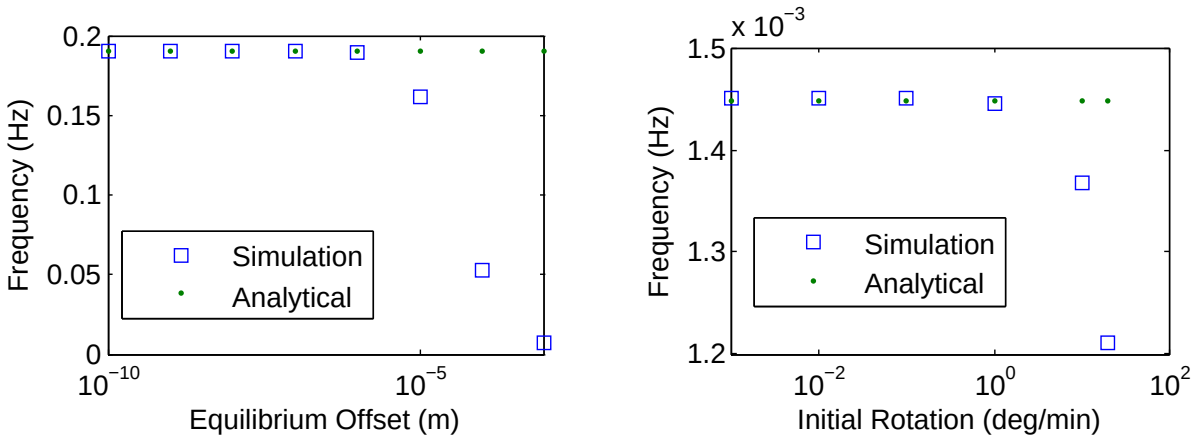

(a) Translational Frequency (b) Rotational Frequency

Figure A.2: Frequency comparison between simulation and analytics

A.2 Tether Model Comparison

The numerical simulation for the dynamic modeling of TCS systems models a tether as a proportional spring with non-linear end displacements. This simplified model is used to allow for

increased speed in simulation. A higher fidelity finite element model (FEM) was used to model TCS tethers as well. Identical simulations were run using both models. A comparison of the two models effects on rotation and tether tension is given in Figure A.3. The results of each simulation are not expected to be exactly equal, but close. The simulations were conducted with the single-tether two-node rotational TCS configuration in Figure 3.2 with the parameters of Table 3.2. However, the inertia of the craft is modeled as a disk and the initial rotation is 30 deg/min. Additionally, for this comparison a simplified charge model of

$$V_i = \frac{q_i k_c}{\rho}$$

is used because the FEM model is not currently incorporating Equation 2.7. From the figure it can be seen that both models provide nearly identical rotations and tensions. The FEM model however, does provide slightly large force magnitudes as well as allows for compression in the tethers. Even so, the results of Figure A.3 show that the simplified tether model used in this work is acceptable.

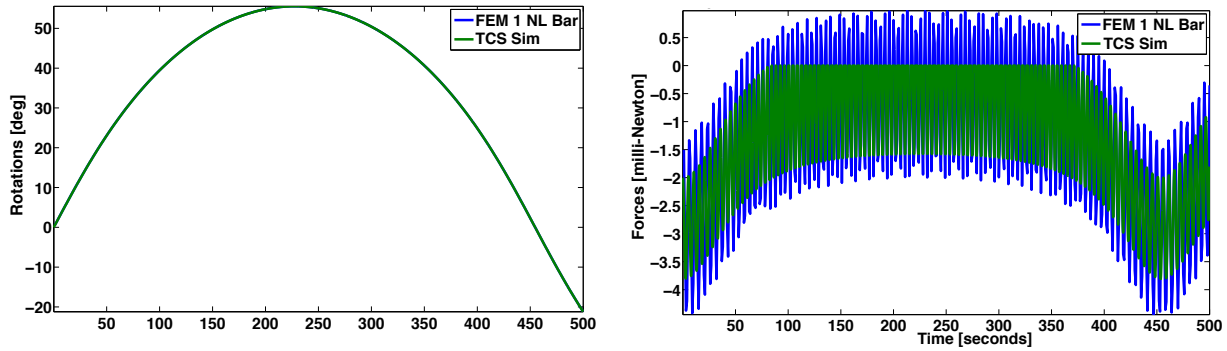

(a) Node Rotation

(b) Tether Tension

Figure A.3: Comparison of tether model simulation results